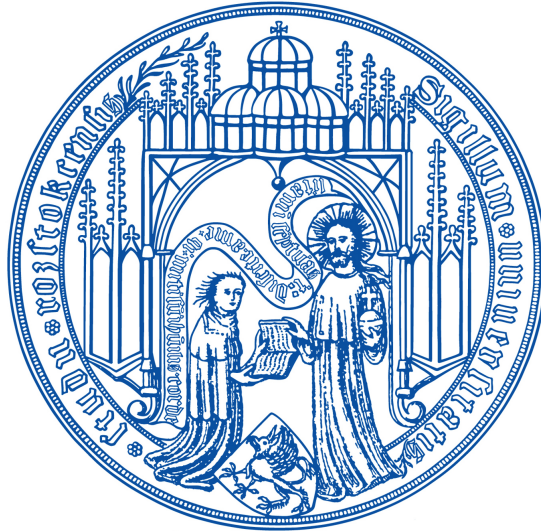# Numerical simulations of estuarine circulation in a non-tidal estuary

written at the Leibniz Institute for Baltic Sea Research Warnemünde
Partner Institut of the mathematical-scientific faculty
of the University of Rostock

Rostock, 09th of October 2015

Xaver Lange, born 19th of March 1991 in Stralsund

supervisor and 1st auditor : Prof. Dr. Hans Burchard, IOW
2nd auditor : Prof. Dr. Gerald Schernewski, IOW

Contents

Abstract

This thesis explores estuarine circulation processes of a non-tidal estuary using the example of the Warnow, a river mouth in the western Baltic Sea. By means of the 3d coastal ocean model GETM (General Estuarine Transport Model) highly resoluted simualtions under idealized and realistic conditions are executed and compared with known and new solved analtical solutions.

1   Introduction

The Warnow is with a route of 155 km the second longest river in Mecklenburg-Western Pomerania. The last section before the river flows into the Bay of Mecklenburg is called Unterwarnow, which is, conditioned by the strategic location, the lifeline of the Hanseatic City of Rostock from medieval times to the present.

Historical map of Rostock and the Unterwarnow, 1788

Figure 1: „Rostock 1788" by Friedrich Wilhelm von Schmettau - F. Mohr, G. Stentzel: Rostocker Stadtbilder, Rostock 2005, page 29.

The Unterwarnow and the Oberwarnow are separated by a lock, which parts the freshwater of the Oberwarnow from the brackish water of the Unterwarnow. This separation exists since the Middle Ages where a weir was installed to operate water mills. The oldest known illustration of locks at the Mühlendamm from the year 1653 can be seen in figure 2. The spatial separation of these two river systems is important today, too, because the drinking water in Rostock is obtained from the surface water of the Oberwarnow. Since 2011 the lock operation folded due to renovation of the Mühlendamm-bridge and there are no plans to re-establish the service.
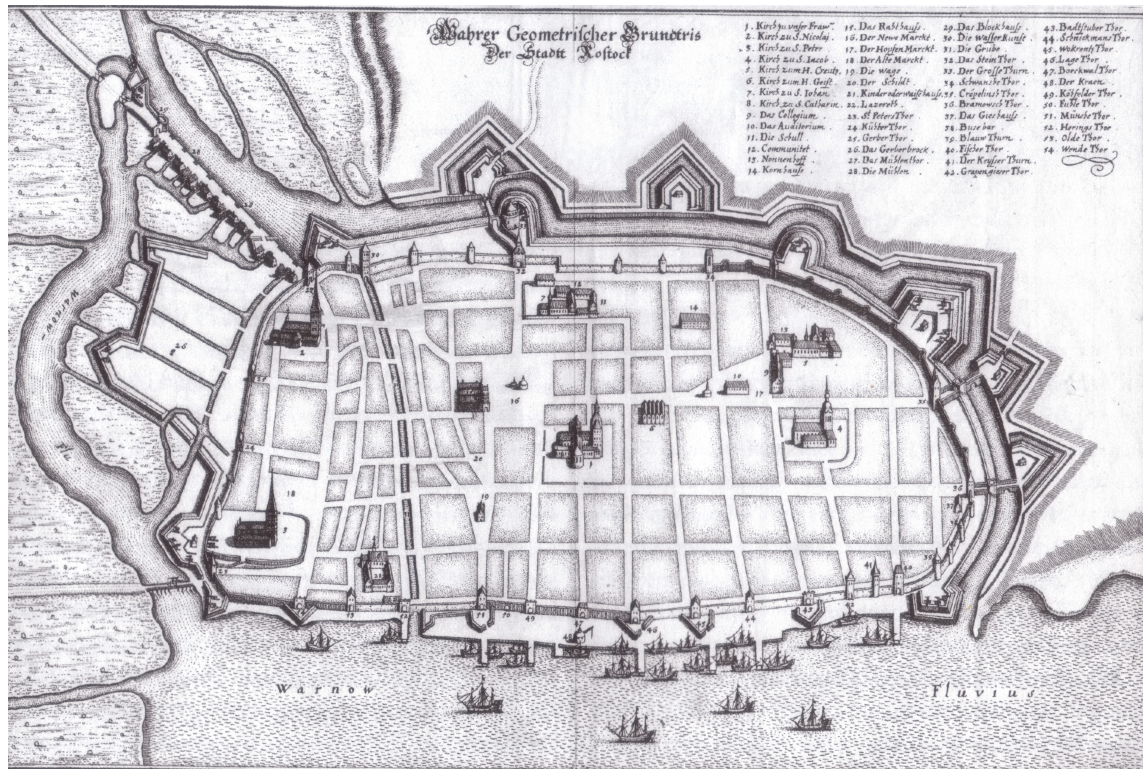
Historical map of Rostock, 1653

Figure 2: Historical draft of Rostock from the year 1653 showing the oldest known illustration of locks and weirs installed at the Warnow (top left). „Rostock Merian" by Caspar Merian.Licensed under Public Domain via Commons - https://commons.wikimedia.org/wiki/File:Rostock_Merian.jpg

Through the installed weir the volume flux of the river is regulated. The time series of the freshwater inflow Q compared with the water levels of the Unterwarnow and the Oberwarnow are shown in figure 3 for the month March, 2014. As can be seen the river systems are decoupled. While the water level of the Oberwarnow (in blue) is tried to hold at a constant height the sea surface of the Unterwarnow rises and falls conditioned by the tides and the water level of the Baltic Sea. Therefore the volume flux doesn't becomes greatest at times of high differences of the surface height, but rather is regulated down to ensure a constant level before the weir. In the following the names Warnow and Unterwarnow will be used synonymously.

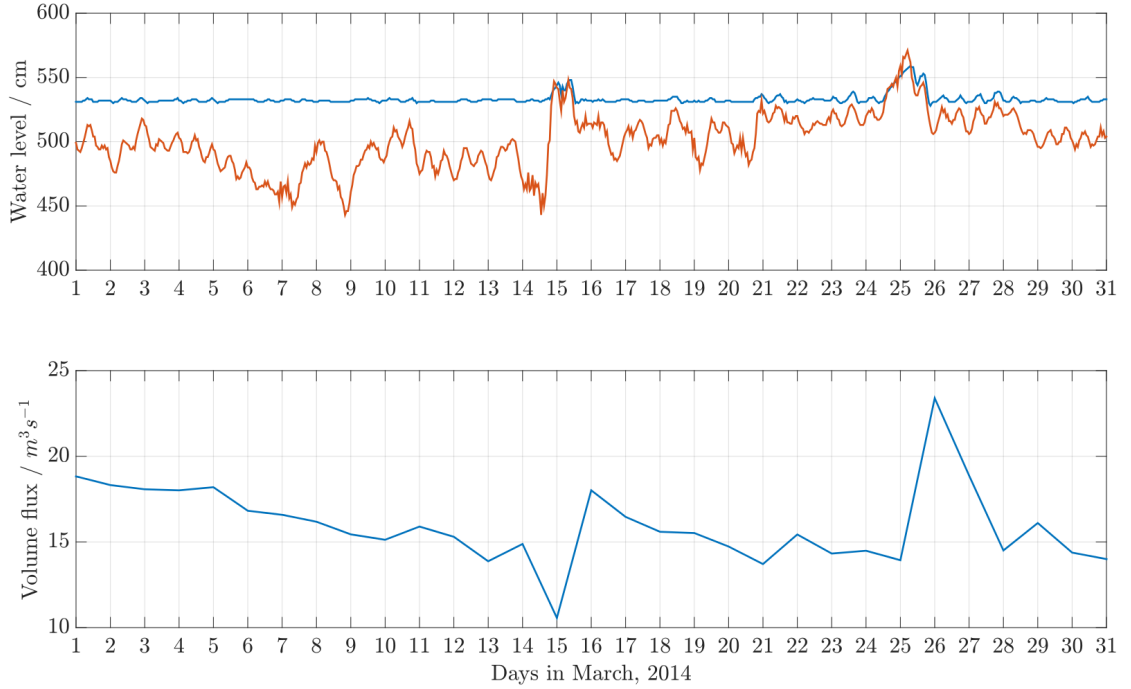**Surface elevations before and behind the weir in cm**

Figure 3: Warer level in cm of the Unterwarnow compared to the Oberwarnow (upper panel). The surface height before the weir is hold nearly constant, while the surface elevation of the Unterwarnow is changed by tides and the warter level of the Baltic Sea. The difference is regulated by the volume flux of the river.

The mouth of the river is located in Warnemünde, a district of Rostock, where the Warnow flows into the Bay of Mecklenburg. Formerly a small fishing village, founded in about 1200, it was purchased by the city of Rostock in 1323 to ensure its access to the Baltic Sea. For centuries the shape of the harbour has been adjusted to the needs of the region. An overview about a reconstructed historical route can be seen in figure **??**. Nowadays the waters are used for the international port, the cruise port, the cargo and fishing port together with several smaller facilities. Therefore a shipping channel is applied with its greatest depth at 18 m. Through this channel salty ocean water reaches the estuary and spreads over the whole river.

An estuary in the context of the Warnow is characterised by the crossover of a river system with the adjoining ocean. In the embayment of the coast less of salinity is present compared to the ocean's water due to freshwater inflow of the river. The resulting horizontal density gradient forces a horizontal pressure gradient, which tries to flatten the isopycnals, just as the sea surface slope. This leads to an upriver current transporting dense shelf water into the river below the outflowing surface layer. This bidirectional flow is called estuarine circulation or exchange flow. Beside the density gradient turbulent mixing is crucial, mainly driven by wind straining and tidal currents. The latter can be studied on the basis of time series of the water level. In figure 4 the surface elevation in Warnemünde in blue and the running average over one day in red is given in the upper panel for the months August and September. The semidiurnal tide (M2) is visible to the unaided eye. The differences between the curves (lower panel) show a tidal amplitude of 10 - 20 cm. Therefore the influence of tides on processes of the Warnow is minor compared to estuaries like that of the Elbe. Further modes can be guessed due to the envelope of the beat. The Fourier transformation of the surface elevation of a time series over 15 years showed several
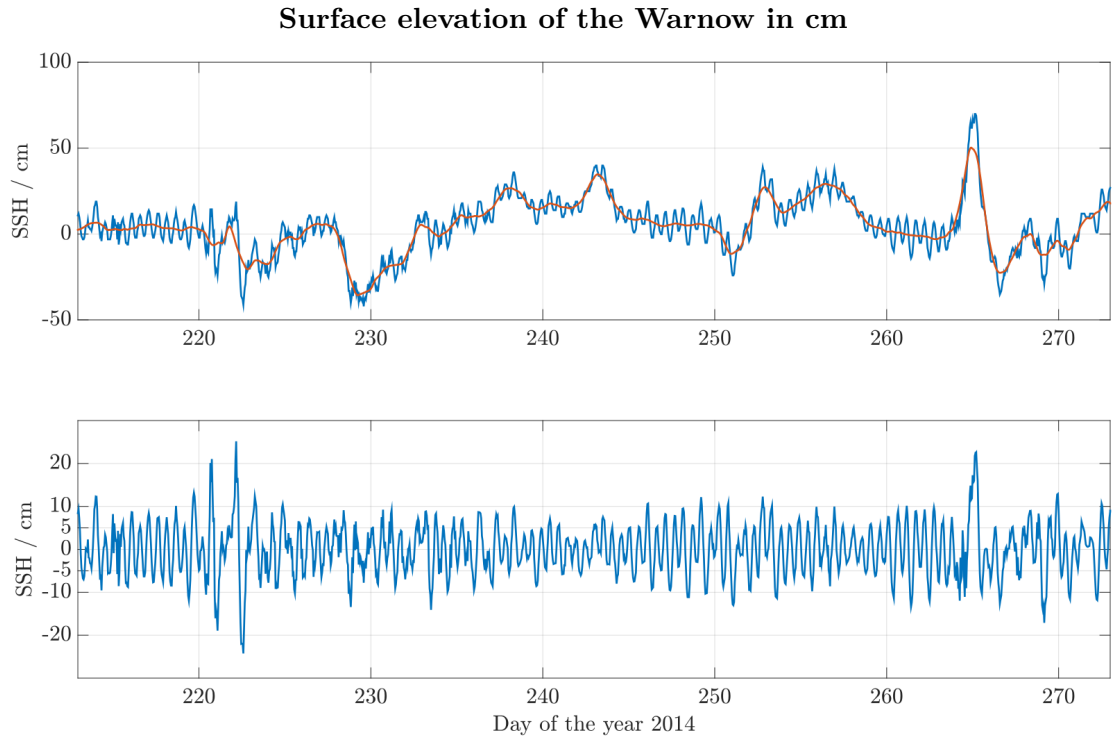
Surface elevation of the Warnow in cm

Figure 4: Surface elevation of the Warnow in blue and the averaged progression in red for the months August and September (upper panel). The semidiurnal tide caused by the moon is clearly visible. The differences (lower panel) correspond to a tidal amplitude of 10 - 20 cm.

tidal modes. A selection can be seen in figure 5. Due to the long hourly resolved period of measurements even weak tidal modes can be observed.

Fourier transformation of the surface elevation

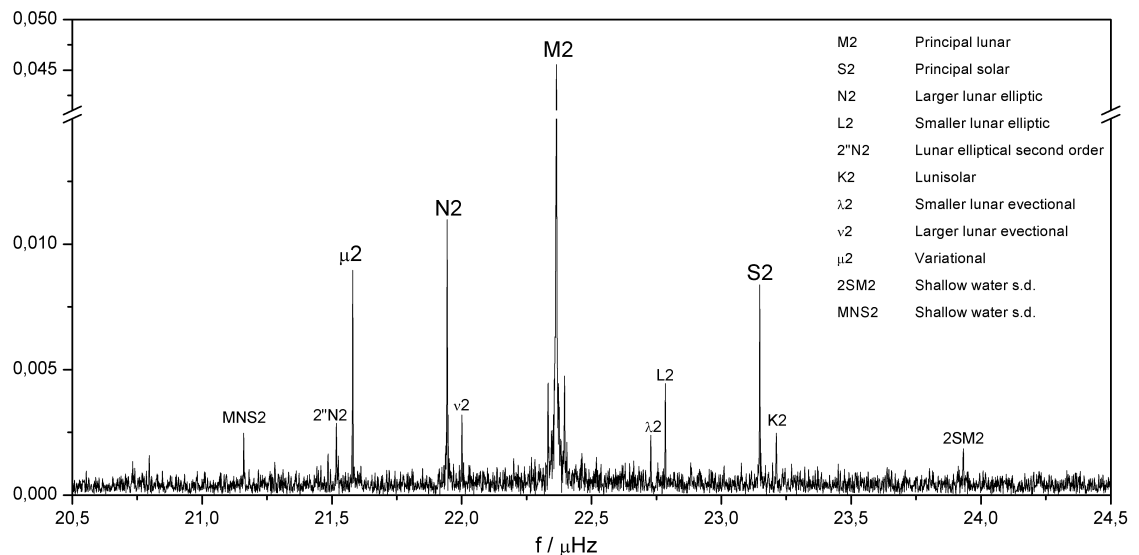| M2 | Principal lunar |
S2	Principal solar
N2	Larger lunar elliptic
L2	Smaller lunar elliptic
2"N2	Lunar elliptical second order
K2	Lunisolar
λ2	Smaller lunar evectional
ν2	Larger lunar evectional
μ2	Variational
2SM2	Shallow water s.d.
MNS2	Shallow water s.d.

Figure 5: Fourier transformation of a long-term surface elevation measurement of the Warnow. Even small tidal modes can be proved due to the long integration time.
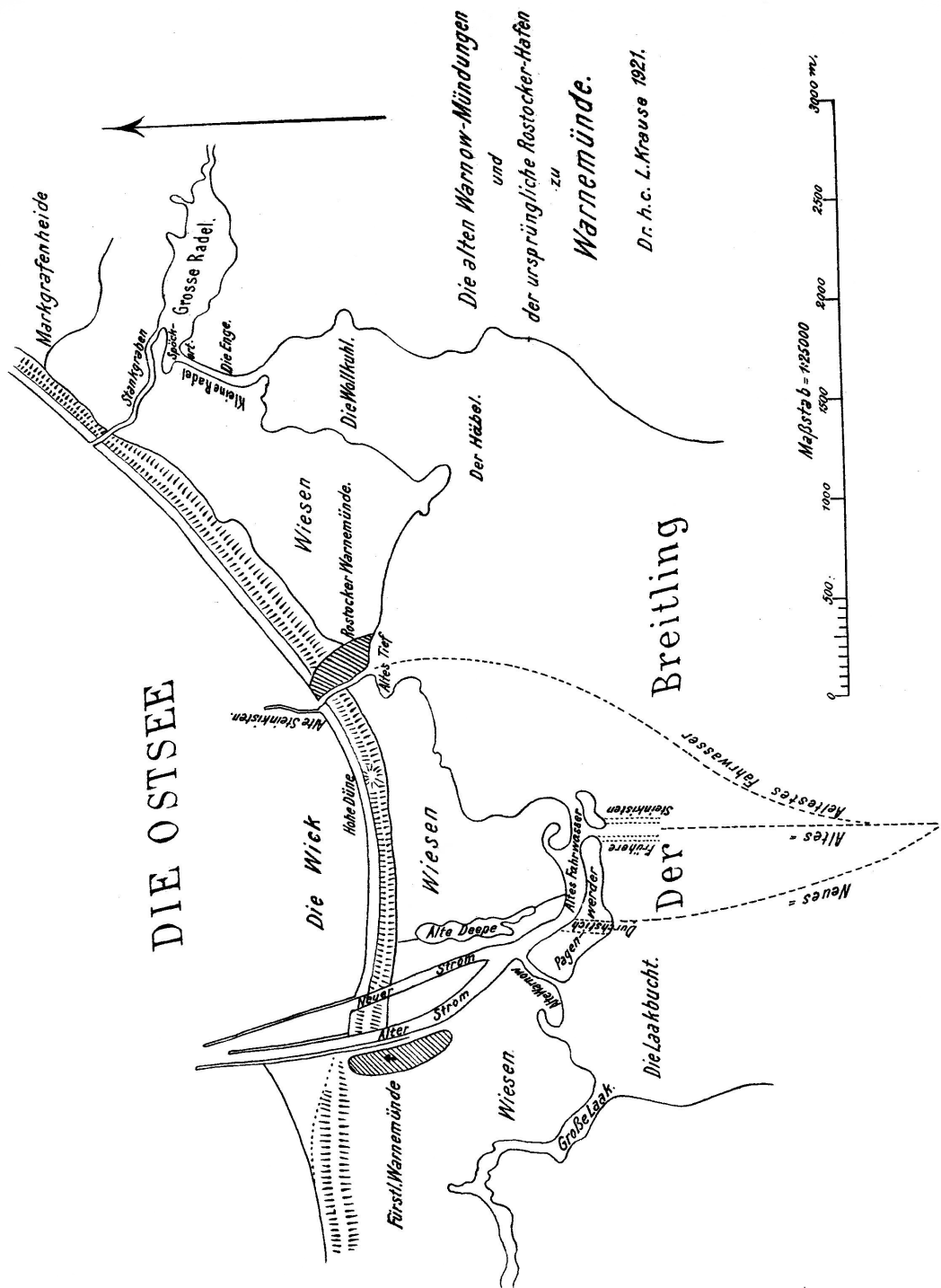
Figure 6: Reconstructed historical route of the upper part of the Warnow. Dr. h.c. L. Krause - Beiträge zur Geschichte der Stadt Rostock. Hrsg. v. Verein für Rostocks Altertümer. Zwölfter Band (Jahrgang 1920-1923). Rostock 1924.

2 Theory

In order to get an idea of the mechanisms behind the dynamics of an estuarine flow, some mathematical and physical relations are presented. First, the Navier-Stokes equation for incompressible fluids will be derived from material properties and basic laws of continuum mechanics. Subsequently a solution for simplified and advanced conditions will be derived and studied.

2.1 Basic framework

Let us assume a Cartesian coordinate system on the rotating earth with the x coordinate pointing eastward, the y coordinate pointing northward and the z coorinate pointing upward with its origin at the mean sea surface height. The time derivative of the position vector may be written as $\underline{u} = (u, v, w)$. From the law of mass conservation, the assumption of an incompressible fluid can be expressed as

$$\nabla \cdot \underline{u} = 0 \quad , \tag{1}$$

which is reasonable as long as the considered velocities are much smaller than the speed of sound. Newton's second law (conservation of momentum) can be written in differential notation as:

$$\mathrm{d}\underline{F} = \mathrm{d}m \frac{\mathrm{d}\underline{u}}{\mathrm{d}t} = \rho \mathrm{d}V \left(\partial_t \underline{u} + (\underline{u} \cdot \nabla) \, \underline{u} \right) \quad . \tag{2}$$

Equation (2) can be rewritten by introducing the specific force $f_i = \mathrm{d}F_i / \mathrm{d}m$, which consists of inner and outer force components:

$$\partial_t \underline{u} + (\underline{u} \cdot \nabla) \, \underline{u} = \underline{f}^i + \underline{f}^o \quad . \tag{3}$$

Internal forces transport momentum due to frictional effects described by the viscous stress tensor $\underline{\underline{\sigma}} = -p\underline{\underline{1}} + \underline{\underline{\tau}}$. By using of (1), the shear stress $\tau_{ij} = \mu \left(\partial_{x_j} u_i + \partial_{x_i} u_j \right)$ and the kinematic viscosity $\nu = \mu / \rho_0$, the force can be written as

$$\underline{f}^i = \frac{1}{\rho_0} \mathrm{div} \underline{\underline{\sigma}} = -\frac{1}{\rho_0} \nabla p + \nu \Delta \underline{u} \quad . \tag{4}$$

In this setup the external forces consist of gravity and the Coriolis force, as a result from coordinate transformation on a rotating frame of reference. With the assumption that the density only varies in the gravitational term (*Boussinesq approximation*) the outer forces can be written as

$$\underline{f}^o = \underline{g} \frac{\rho}{\rho_0} - 2\underline{\Omega} \times \underline{u} \quad , \tag{5}$$

with the gravity factor g, the density *rho* and the Coriolis frequency. This leads to the Navier-Stokes equation for incompressible flow

$$\partial_t \underline{u} + (\underline{u} \cdot \nabla) \, \underline{u} + 2\underline{\Omega} \times \underline{u} = -\frac{1}{\rho_0} \nabla p + \underline{g} \frac{\rho}{\rho_0} + \nu \Delta \underline{u} \quad . \tag{6}$$

Following the work of Reynold (1895), the variables in (6) are decomposed into a mean and a fluctuating component $X = \langle X \rangle + X'$, where the angular brackets denote an ensemble average with the properties $\langle X' \rangle = 0$ and $\langle \langle X \rangle \rangle = \langle X \rangle$. If further the horizontal scales are assumed to be much greater than the vertical scales (*shallow water assumption*), the components of (6) can be written with the Coriolis parameter $f = 2\Omega \sin(\phi)$ as

$$\partial_t \langle u \rangle + \underline{u} \cdot \nabla \langle u \rangle - f \langle v \rangle = -\frac{1}{\rho_0} \partial_x \langle p \rangle + \partial_z \left(\nu \partial_z \langle u \rangle - \langle u' w' \rangle \right) \quad , \tag{7}$$

$$\partial_t \langle v \rangle + \underline{u} \cdot \nabla \langle v \rangle + f \langle u \rangle = -\frac{1}{\rho_0} \partial_y \langle p \rangle + \partial_z \left(\nu \partial_z \langle v \rangle - \langle v'w' \rangle \right) \quad , \tag{8}$$

$$\partial_z \langle p \rangle = -g \langle \rho \rangle \quad , \tag{9}$$

where ϕ denotes the geographical latitude. The vertical stress $\langle u'w' \rangle$ in (7), or equivalently named vertical Reynolds stress, has the meaning of a vertical turbulent momentum flux and is often expressed in an analogue way to the molecular viscosity in terms of a vertical turbulent viscosity ν_t:

$$\langle u'w' \rangle = -\nu_t \partial_z \langle u \rangle, \quad \langle v'w' \rangle = -\nu_t \partial_z \langle v \rangle \quad . \tag{10}$$

The physics of the turbulent flow is therefore downscaled to an expression for the eddy viscosity ν_t, which depends on the shear of the velocity and the distance to the wall. This is explained more detailed in chapter 2.3.

From now on the angular brackets will be dropped for simplicity. Equation (9) is known as *hydrostatic balance*. Vertically integrated from an arbitrary position z in the water column up to the free surface elevation η and subsequently horizontally derivated, the pressure gradient in (7) and (8) can be expressed by use of the Leibniz integration rule in terms of the barotropic pressure gradient, baroclinic pressure gradient and atmospheric pressure gradient (from left to right):

$$-\frac{1}{\rho_0} \nabla^h p = -\frac{\rho(\eta)}{\rho_0} g \nabla^h \eta - \frac{g}{\rho_0} \int_z^\eta \nabla^h \rho \, dz' - \frac{1}{\rho_0} \nabla^h p_a \quad , \tag{11}$$

with the atmospheric pressure $p_a = p(\eta)$ and the horizontal derivation operator ∇^h. The expression $\rho(\eta)/\rho_0$ becomes unity under Boussinesq approximation.

The potential density is described by a semi-empirical relation of salinity S, potential temperature θ and pressure p (*equation of state*). A linearised form of TEOS-10 (International Thermodynamic Equation of Seawater - 2010), following from the thermodynamics of viscous fluids, with the constant reference values for density, temperature and salinity ρ_0, θ_0 and S_0 is frequently used in analytical solutions for simplicity

$$\frac{\rho}{\rho_0} = 1 - \alpha(\theta - \theta_0) + \beta(S - S_0) \quad , \tag{12}$$

with the thermal expansion coefficient $\alpha = (\partial \rho / \partial \theta)_{S,p} / \rho_0$ and the haline contraction coefficient $\beta = (\partial \rho / \partial S)_{\theta,p} / \rho_0$. Typical values for seawater are in the order of $\alpha = 2 \cdot 10^{-4}$ K^{-1}, $\beta = 8 \cdot 10^{-4}$ kg/g and $\rho_0 = 1025$ kg/m^3. Therefore the governing equation for the u-velocity can be written as

$$\partial_t u + \underline{u} \cdot \nabla u - fv = -g \partial_x \eta + \int_z^\eta \partial_x b \, dz' - \frac{1}{\rho_0} \partial_x p_a - \partial_z \left((\nu + \nu_t) \partial_z u \right) \quad , \tag{13}$$

where the buoyancy $b = -g(\rho - \rho_0)/\rho_0$ is introduced. At the surface and the bottom von Neumann boundary conditions for the momentum flux can be formulated, named *dynamic boundary conditions*:

$$-\underline{\tau}^s = \rho_0 \nu \partial_z \underline{u} \mid_{z=\eta} \quad \text{and} \quad \underline{\tau}^b = \rho_0 \nu \partial_z \underline{u} \mid_{z=-H} \quad , \tag{14}$$

with the surface stress $\underline{\tau}^s$ and the bottom stress $\underline{\tau}^b$. Here is assumed that momentum fluxes entering the fluid are counted as positive. The surface stress is caused by interaction with

the atmosphere and is often parameterized in terms of the wind velocity in a height of 10 m above the sea surface:

$$\underline{\tau}^s = \underline{\tau}_w = \rho_{\text{air}} \cdot C_D \cdot \underline{u}_{10}|\underline{u}_{10}| \quad , \tag{15}$$

with the density of air ρ_{air} and the dimensionless drag coefficient C_D. Further boundary conditions resulting from kinematic arguments which are independent from the material properties of the fluid are named *kinematic boundary conditions*:

$$w(\eta) = \partial_t \eta + u(\eta)\partial_x \eta + v(\eta)\partial_y \eta \quad ,$$
$$w(-H) = -u(-H)\partial_x H - v(-H)\partial_y H \quad . \tag{16}$$

2.2 Solution for simplified estuarine conditions

Similar to the work of Hansen and Rattray (1965) an analytical solution of (13) for density driven flows will be derived.

Considering stationary solutions without Coriolis effects and neglecting non-linear terms and kinematic viscosity (which is typically several orders of magnitude smaller than the eddy viscosity ν_t), equation (13) reduces with a laterally constant air pressure to

$$\partial_z (\nu_t \partial_z u) = g\partial_x \eta + z\partial_x b \quad , \tag{17}$$

where a temporally and spatially constant pre-described density gradient is assumed. Integration from an arbitrary position to the zero mean sea surface leads to

$$\partial_z u = \frac{g\partial_x \eta}{\nu_t} z + \frac{\partial_x b}{2\nu_t} z^2 + \frac{\tau_w}{\nu_t \rho_0} \quad , \tag{18}$$

where the wind stress τ_w is used as a boundary condition as described in equation (14). Equation (18) can be integrated from the bottom $-H$ to the position z by the usage of a constant eddy viscosity, which reduces with the *no-slip condition* $u(-H) = 0$ to

$$u(z) = \frac{g\partial_x \eta}{\nu_t} \left(\frac{1}{2}z^2 - \frac{1}{2}H^2 \right) + \frac{\partial_x b}{2\nu_t} \left(\frac{1}{3}z^3 + \frac{1}{3}H^3 \right) + \frac{\tau_w}{\nu_t \rho_0} (z + H) \quad . \tag{19}$$

The sea surface slope can be eliminated by introducing the *residual flow*

$$u_r = \frac{1}{H} \int_{-H}^{0} u(z)dz, \tag{20}$$

which leads to the classical solution with the dimensionless depth $\xi = z/H$

$$u(\xi) = \frac{\partial_x b H^3}{48\nu_t} \left(8\xi^3 + 9\xi^2 - 1 \right) + \frac{3}{2}u_r \left(1 - \xi^2 \right) + \frac{\tau_w H}{4\nu_t \rho_0} \left(3\xi^2 + 4\xi + 1 \right) \quad . \tag{21}$$

Therefore the velocity profile is governed by the horizontal density gradient, the effective volume flux $Q = u_r A$ and wind straining, with the cross-section area A. Equation (21) can be rewritten in a non-dimensional velocity shape by introducing the exchange and the wind coefficient $u_e = \partial_x b H^3/48\nu_t$ and $u_w = \tau_w H/4\nu_t \rho_0$:

$$\frac{u}{u_e} = \left(8\xi^3 + 9\xi^2 - 1 \right) + \frac{u_r}{u_e} \left(\frac{3}{2} - \frac{3}{2}\xi^2 \right) + \frac{u_w}{u_e} \left(3\xi^2 + 4\xi + 1 \right) \quad . \tag{22}$$

Therefore the physics depends only on the ratios u_r/u_e and u_w/u_e.

In Figure 7 the terms of solution (22) are shown for varying ratios of u_r/u_e and u_w/u_e. The profile of the residual flow behaves like the classical solution for laminar flow with molecular viscosity. The freshwater inflow's portion of the resulting residual velocity is by itself not very high (for example $u_{r,fresh} \approx 0.01$m/s for the Warnow) but the freshwater inflow of the river in interaction with the ocean water is relevant for the density gradient $\partial_x b$. The resulting baroclinic pressure gradient is responsible for a near-bottom upriver current, transporting salty ocean water into the estuary. This affects the contribution of density and therefore the stratification. Along estuary wind stress amplifies the density driven flow, while a wind field with the opposite sign counteracts and works destratificationally.

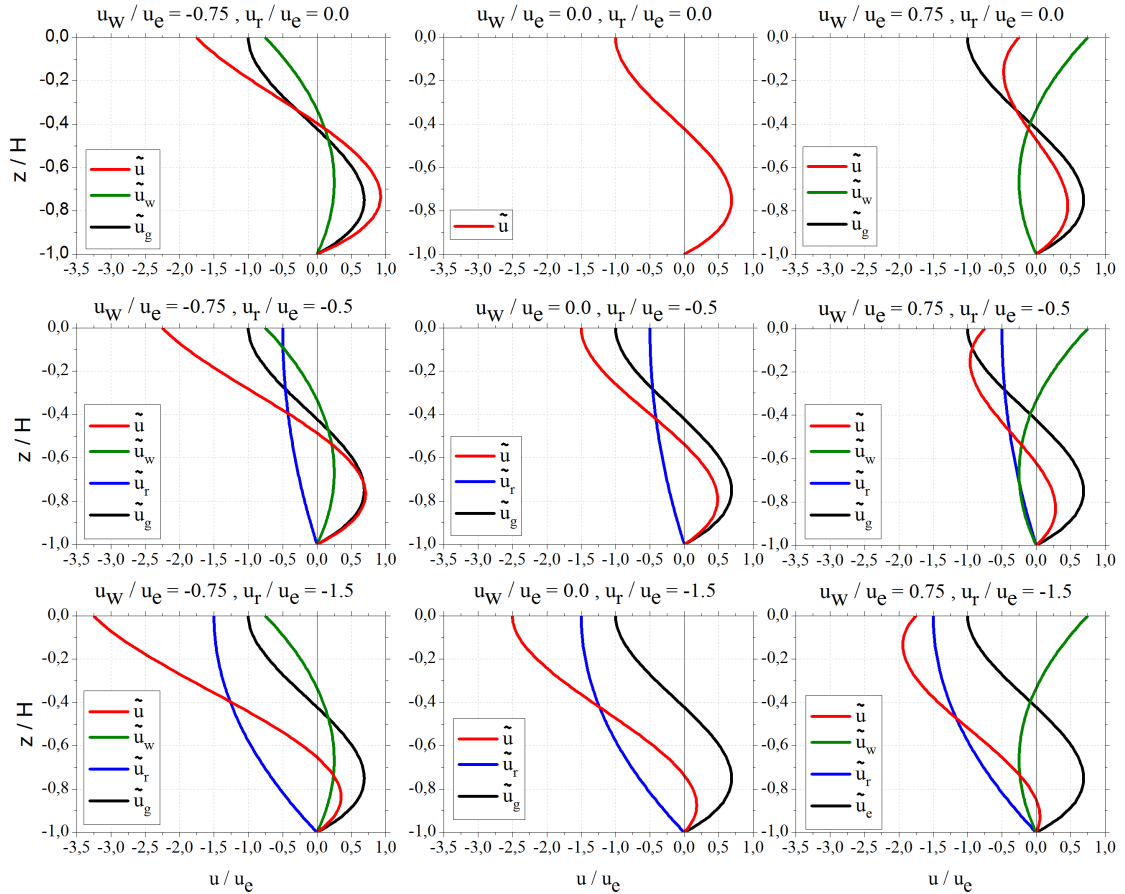**Dimensionless velocity profiles for varying parameters**

Figure 7: Dimensionless water velocity profiles u/u_e in red for varying ratios of u_r/u_e in blue and u_w/u_e in green. The water column can be subdivided into a surface layer with downriver currents and a layer with an upriver flow near the bottom. This effect can be amplified or damped by wind straining, depending on its direction.

2.3 Treatment of turbulent diffusivity

Equation (18) is solved in section (2.2) with the assumption of a constant eddy viscosity ν_t, which is useful to discover the main contributors to estuarine circulation. A more realistic result is obtained with a parabolic profile for the turbulent viscosity. The size of energized eddies grows linearly with the distance to the wall, so that the turbulent viscosity grows linearly, too, if a constant shear stress in the boundary layer is assumed. This motivates the parametrisation of the viscosity at the bottom as a product of a turbulent velocity scale (bottom friction velocity u_*^b) and a turbulent length scale (bottom roughness z_0^b), analogous to the molecular viscosity in the kinematic theory of gases. Interpolation between the surface layer and the bottom results in

$$\nu_t = \kappa |u_*^b|(z + z_0^b + H)\left(-\frac{z}{H}\right) \quad , \tag{23}$$

with the Kármán constant $\kappa = 0.4$. The bottom friction velocity can be obtained from the periodic tidal cycle (Burchard et al. (2011)) with the non-dimensional roughness $\tilde{z}_0^b = z_0^b/H$:

$$C_D = 2\left(\frac{u_*^b}{U_2}\right)^2 = \frac{\kappa^2}{((1+\tilde{z}_0^b)\ln[1/\tilde{z}_0^b + 1] - 1)^2} \quad , \tag{24}$$

wherefore $|u_*^b|$ becomes a small value in this thesis due to the minor value of the semidiurnal current velocity amplitude U_2 in the Warnow. Equation (18) without wind straining is then solved with a parabolic turbulent viscosity by (Burchard and Hetland, 2010)

$$u_{\tau_w=0} = \frac{\partial_x b H^2}{2\kappa |u_*^b|}\left[\frac{1}{2C}\ln\left(\frac{z+H+z_0^b}{z_0^b}\right) - \left(\frac{z}{H}+1\right)\right] + \frac{1}{C}\ln\left(\frac{z+H+z_0^b}{z_0^b}\right)u_r \quad , \tag{25}$$

with the constant

$$C = \frac{1}{H}\int_{-H}^{0}\ln\left(\frac{z+z_0^b+H}{z_0^b}\right)\mathrm{d}z = \frac{H+z_0^b}{H}\ln\left(\frac{H+z_0^b}{z_0^b}\right) - 1 \quad . \tag{26}$$

An extension of (25) with wind straining is firstly presented in this thesis:

$$u = u_{\tau_w=0} - \frac{\tau_w}{\rho_0\kappa|u_*^b|}\frac{H}{H+z_0^b}\left(\ln\left(\frac{z}{-H}\right) + \frac{1}{C}\ln\left(\frac{z+H+z_0^b}{z_0^b}\right)\right) \quad . \tag{27}$$

A detailed derivation of equation (27) is given in appendix I. This solution is solved with the assumption of a missing roughness length at the surface, leading to an infinite velocity at $z = 0$. If the viscosity in equation (23) is extended with a non-zero z_0^s, equation (18) is not any longer analytically solvable. Because typical surface roughness lengths are in the order of 10^{-4} m to 10^{-3} m over the sea and therefore close by zero, equation (27) leads to reasonable results along the water column except for a water layer at the surface.

The residual flow u_r consists of the river inflow Q/A, but is also affected by momentum input due to the barotropic pressure gradient, density gradient and wind stress:

$$u_r = -\frac{g\partial_x\eta H}{\kappa|u_*^b|}C + \frac{\partial_x b H^2}{2\kappa|u_*^b|}\left(\frac{z_0^b+H}{H}C - \frac{1}{2}\right) + \frac{\tau_w}{\rho_0\kappa|u_*^b|}\frac{H}{H+z_0^b}(1+C) \quad . \tag{28}$$

A dimensionless form of equation (27) can be reached by dividing it by $|u_*^b|$, which reads as follows:

$$\frac{u}{|u_*^b|} = \frac{\text{Si}}{2\kappa} \left(\frac{\ln\tilde{Z}}{2C} - (\xi + 1) \right) + \tilde{u}_r \frac{\ln\tilde{Z}}{C} - \tilde{u}_w \frac{C_D^{\text{air}}\rho_{\text{air}}}{\kappa\rho_0} \frac{1}{1 + \tilde{z}_0^b} \left(\ln(-\xi) + \frac{\ln\tilde{Z}}{C} \right) \quad , \qquad (29)$$

with the Simpson number Si$= \partial_x b H^2/(u_*^b)^2$, the dimensionless residual flow velocity $\tilde{u}_r = u_r/|u_*^b|$, the dimensionless wind velocity $\tilde{u}_w = u_{10}|u_{10}|/(u_*^b)^2$, the non-dimensional bottom roughness $\tilde{z}_0^b = z_0^b/H$ and the depth parameter $\tilde{Z} = (\xi + 1 + \tilde{z}_0^b)/\tilde{z}_0^b$.

In figure 8 - 10 the dimensionless velocity solutions from equation (29) are shown for varying parameters. The Simpson number is ranged from Si=0 (no density gradients) in the uppermost panel to Si=5 in the lowest panel. Wind profiles in green in down-estuary direction are shown on the left side and in up-estuary direction on the right side. The amplitude of the non-dimensional residual flow in blue is shown for moderate conditions in figure 8. The behaviour of this profile is quite different from the one with constant eddy viscosity in figure 7. The logarithmic dependence on water depth is known as *law of the wall*. The resulting dimensionless velocity profile in red is compounded by a superposition of the residual flow, wind straining and the influence of density gradients. The middle row in figure 8 shows the case, where the terms are added so that there exists no upriver current. If the density gradient increases a little, then an upriver current will be found. This can even be obtained if the down river wind velocity increases, which therefore advantaged estuarine circulation. The density gradient has to increase more if the wind is aligned upriver, which therefore counteracts the residual circulation. In realistic cases the residual flow will decrease if the wind is blowing upriver due to the changing sign of the wind stress in equation (28). Therefore a weak density gradient and an upriver wind field can lead to an inverted estuarine circulation. If the density gradient is enhanced the common compensation velocity profile will be obtained (last row). In this case the wind straining affects mainly the upper layer of the water column. The maximum of the upriver flow velocity is located slightly deeper than that of the profile with constant viscosity, which becomes important if transport of sediment or advection of water with higher density is considered. At the bottom every profile by itself fulfils the no-slip condition. If the residual flow is increased, as can be seen in figure 9, the resulting velocity profiles are simply shifted in downriver direction, which decreases the upriver current. In the surface layer the residual flow term becomes relatively constant, while the density gradient terms grow linearly. In figure 10 a less rough bottom is assumed, which mainly increases the near bottom velocities and leads to an almost vertically constant residual flow velocity.
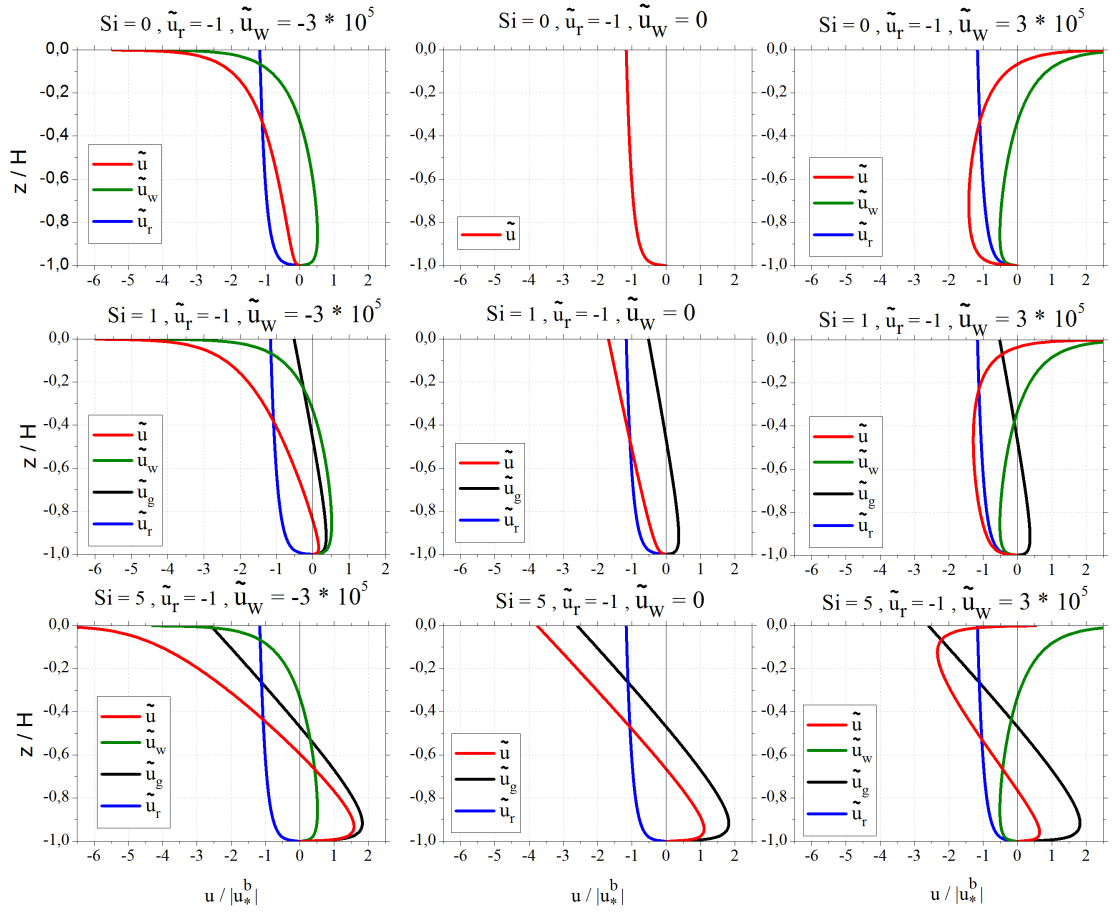
Figure 8: Dimensionless water velocity profiles $u/|u_b^*|$ in red for varied Simpson numbers and non-dimensional wind velocities. The strength of the density gradient driven flow in black increases proportional with increasing Simpson number. The wind induced velocities in green amplify the estuarine circulation if the direction is aligned down river and dampen if oriented upriver. A weak density gradient combined with a sufficient strong upriver wind field results in an inverted water estuarine circulation.
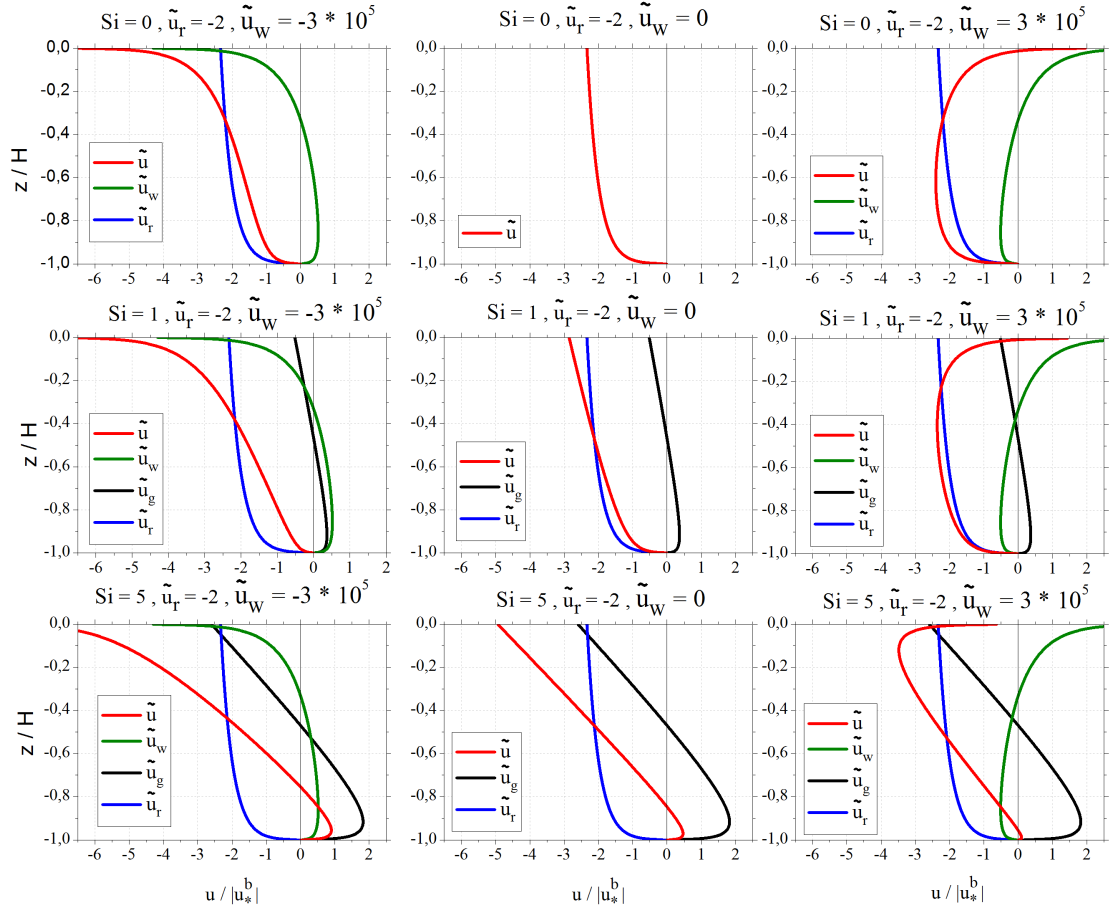
Figure 9: Dimensionless water velocity profiles $u/|u_b^*|$ in red for varied Simpson numbers and non-dimensional wind velocities. The increased residual flow shifts the total velocity.

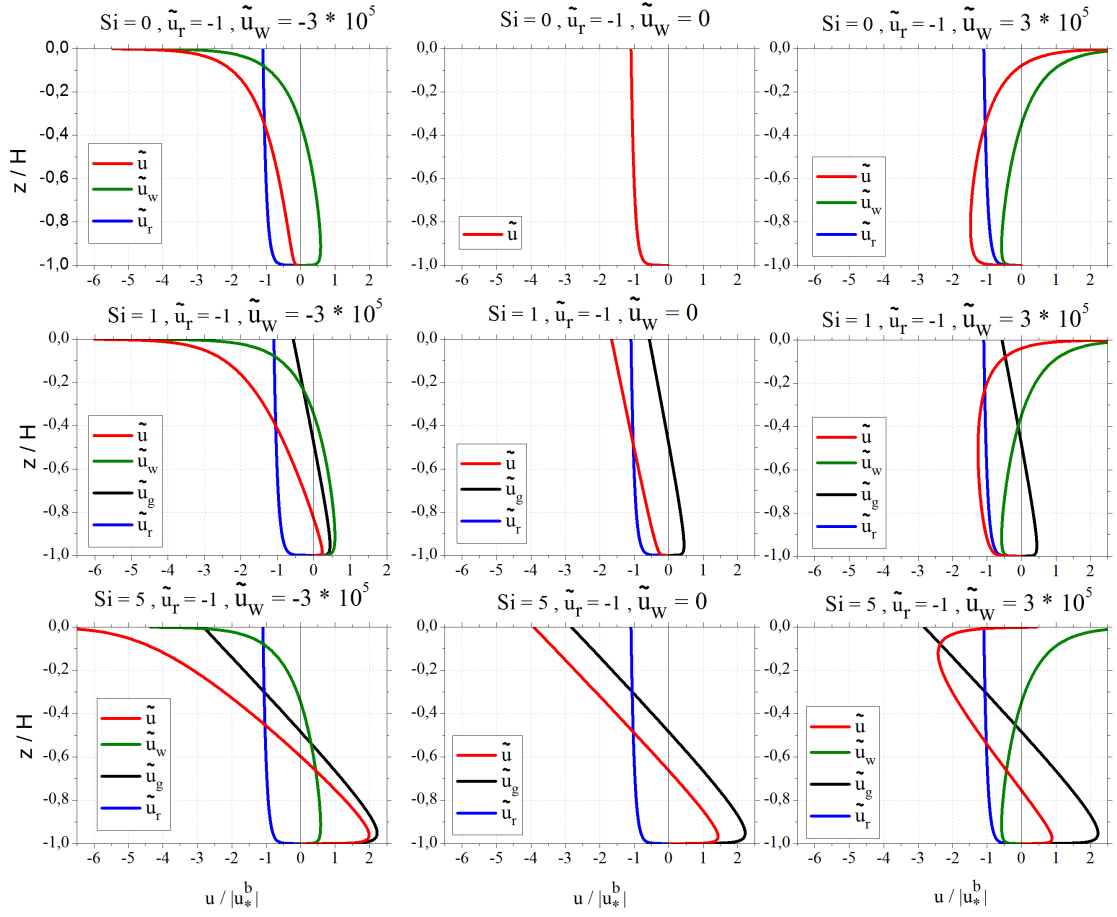**Dimensionless velocity profiles for varying parameters $\tilde{z}_0^b = 10^{-5}$**

Figure 10: Dimensionless water velocity profiles $u/|u_b^*|$ in red for varied Simpson numbers and non-dimensional wind velocities. The reduced bottom roughness changes the bottom near currents.

2.4 Total exchange flow

To quantify the volume fluxes of the in- and outstreaming water MacCready (2011) developed a concept extending the work of Knudsen (1900), based on the contribution of salt in the water column. The isohaline transport function $Q(s, x, t)$ corresponds to the flux of water with a salinity greater than s, with $0 \leq s \leq s_{ocean}$:

$$Q(s, x, t) = \int_{A_s} u(x, t) \mathrm{d}A \quad . \tag{30}$$

The special case $Q(s = 0)$ describes an integral over the full water column and corresponds therefore to the river flux $-Q_R$. With the sign convention, that inflow for a specific salinity class belongs to positive values

$$-\frac{\partial Q}{\partial s}|_{in} > 0 \quad , \tag{31}$$

the particular volume and salt fluxes result from sign-dependent integration:

$$Q_{in} = \int -\frac{\partial Q}{\partial s}|_{in} \mathrm{d}s \quad , \qquad\qquad F_{in} = \int s \left(-\frac{\partial Q}{\partial s} \right) |_{in} \mathrm{d}s \quad , \tag{32}$$

$$Q_{out} = \int -\frac{\partial Q}{\partial s}|_{out} \mathrm{d}s \quad , \qquad\qquad F_{out} = \int s \left(-\frac{\partial Q}{\partial s} \right) |_{out} \mathrm{d}s \quad . \tag{33}$$

The classical Knudsen (1900) relations can be derived from conservation of volume and salt, with $s_{in} = F_{in}/Q_{in}$ and $s_{out} = F_{out}/Q_{out}$:

$$Q_{in} = \frac{s_{out}}{s_{in} - s_{out}} Q_R \quad , \qquad\qquad Q_{out} = -\frac{s_{in}}{s_{in} - s_{out}} Q_R \quad . \tag{34}$$

Therefore the challenging measurement of volume fluxes can be reduced to simple measurements of the distribution of salt (in long-term average).

3 The Model

The numerical simulations of the Unterwarnow were done with the 3D coastal ocean model GETM (General Estuarine Transport Model)(Burchard and Bolding, 2002; Burchard et al., 2004). The physics of the model is based on the three-dimensional hydrostatic Navier-Stokes equations with use of the Boussinesq approximation as displayed in chapter **??**. The vertical velocity component w is calculated by means of the condition of incompressibility (see equation (1)), which ensures the conservation of mass. The kinematic and dynamic boundary conditions from equation (14) and (16) are implemented in GETM just as several conditions for open and closed boundaries at the border of the model.

3.1 Grid and time discretisation

In GETM the C-grid in Arakawa's classification (Arakawa and Lamb, 1977) is used for discretisation of the shallow water equations (see figure (11)).
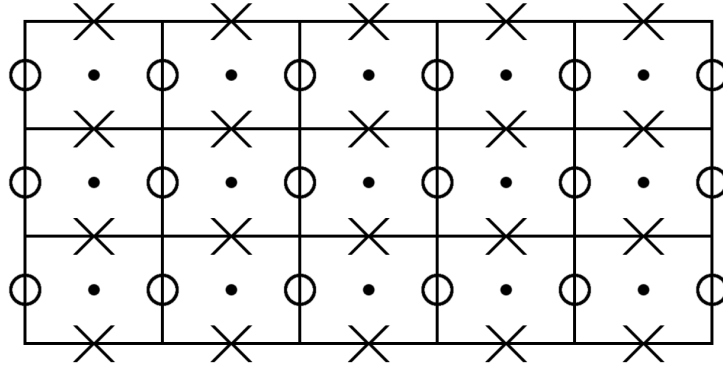

Figure 11: Positions of the evaluation points of the surface elevation $\eta = \bullet$ and the horizontal velocity components $u = \circ$ and $v = \times$. Redrawn from Beckers and Deleersnijder (1993).

For reasons of numerical stability, the Courant-Friedrichs-Lewy condition has to be fulfilled (Beckers and Deleersnijder, 1993):

$$\left(\frac{\Delta t \cdot c}{\Delta x}\right)^2 + \left(\frac{\Delta t \cdot c}{\Delta y}\right)^2 \leq 1 \quad , \tag{35}$$

with the gridspacings Δx and Δy, the micro timestep Δt and the velocity c. Assuming shallow water conditions the barotropic time step is limited by gravity waves $c = \sqrt{gH}$ and therefore by the maximal waterdepth H:

$$\Delta t \leq \frac{\Delta x \Delta y}{\sqrt{gH(\Delta x^2 + \Delta y^2)}} \quad . \tag{36}$$

An increase of Cartesian spatial resolution by halving the horizontal gridspacing and doubling the number of vertical layers, means therefore an increase of physical computation time caused by an eight times higher number of gridpoints and an increase of numerical integration time in the model due to halving the micro timestep. Hence for a bathymetry a reasonable compromise between spatial resolution, memory size and computation time have to be found.

3.2 Bathymetry

The bathymetry of the Unterwarnow and parts of the Bay of Mecklenburg is created from datasets of the Federal Maritime and Hydrographic Agency. The data are interpolated on a Cartesian grid with a spatial resolution of $20\,\mathrm{m} \times 20\,\mathrm{m}$ and implausible values subsequently eliminated. The bathymetry is smoothed by a nine-point smoothing routine for avoiding too large gradients. At the western and northern model boundaries, the bathymetry is adjusted to a $600\,\mathrm{m}$ resolution model of the Baltic Sea, which provides information about elevation, velocity, salt and temperature distributions at those borders. The bathymetry consists of a shipping channel with its greatest depth at $18\,\mathrm{m}$, leading to a micro timestep of $0.75\,\mathrm{s}$.

Mainly three transects are considered in this thesis: a) One at the mouth of the estuary between the pier heads, basically consisting of deeper regions. b) One in the middle of the Unterwarnow with shallow and deeper regions c) a transect generally following the channel from the mouth up to beginning of the Unterwarnow.

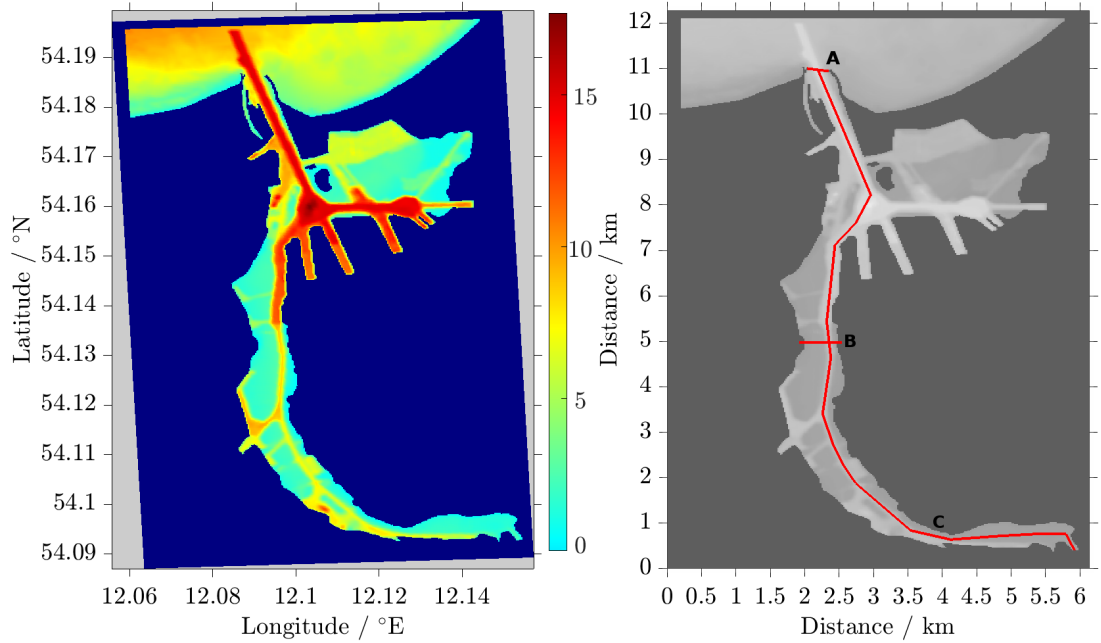**Water depth in m and location of the transects**

Figure 12: Bathymetry of the Unterwarnow (left panel) and location of the considered transects (right panel) at the mouth of the river, in the middle of the Warnow and along the shipping channel. The transects are marked in red.

The transect at the mouth of the river has a cross-section area of $3100\,\mathrm{m}^2$ and is thus nearly twice as big as the transect in the middle of the Warnow with a cross-section area of $1500\,\mathrm{m}^2$. The water column is discretised into 20 layers using equidistant, bottom and surface following sigma coordinates.

The simulations are executed parallelized on a medium sized cluster. The parallelization with MPI (Message Passing Interface) and OpenMP is based on decomposition into subdomains and is therefore well scaleable. The simulations used in this thesis have been done with 47 subdomains, each containing of 48×48 grid points at a setup size of 308×615 grid points.

4 Simplified test cases

In the following some 3D model results for simplified test conditions will be discussed and compared with the analytical solution presented in equation (27). The simulations are executed with the bathymetry of the Warnow from section 3.2 and consider steady-state solutions. The variation parameters are the river volume flux Q, the wind stress τ and the horizontal density gradient $\partial_x b$, while the bottom roughness length z_0^b is set to constant value of $0.01\,\mathrm{m}$.

4.1 Residual flow profiles

First, the influence of the residual flow is considered with varying river volume fluxes Q and without wind stress and density gradients. The water inflow is inserted at the rivers origin downright in figure 12. The analytical vertical velocity profile therefore depends only on the prescribed water depth and the mean velocity given by equation (20). The model results for the case $Q = 10\,\mathrm{m}^3/\mathrm{s}$ are plotted in figure 13 for the estuarine mouth in the left panel and at the middle of the Warnow in the right panel.

Transect velocity in m/s for $Q = 10\,\mathrm{m}^3/\mathrm{s}$
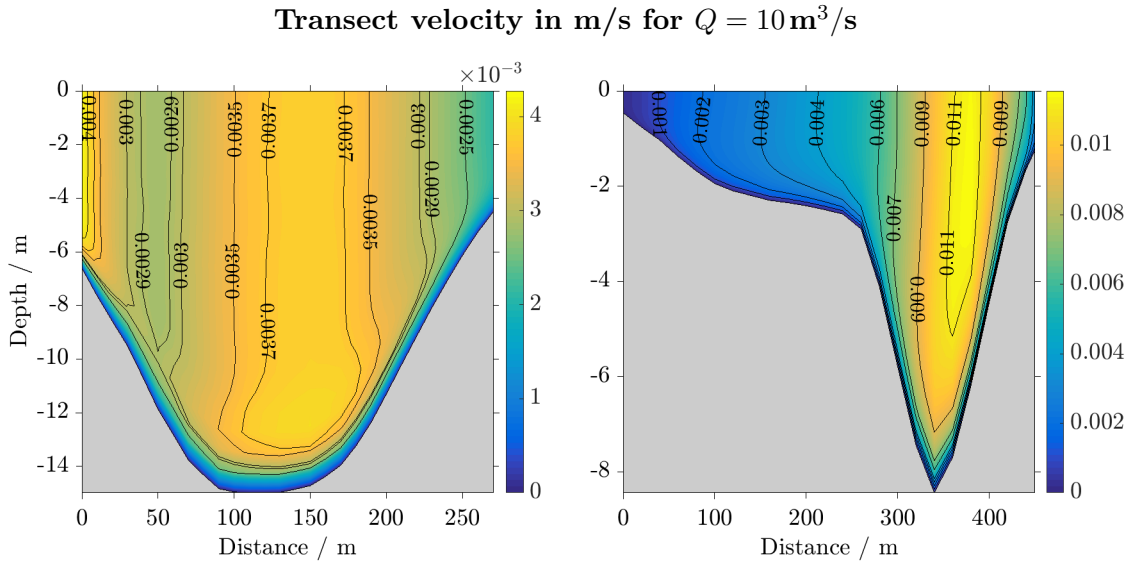

Figure 13: Velocity component perpendicular to the cross-section at the mouth of the river (left panel) and at the middle of the Warnow (right panel) for a river volume flux of $Q = 10\,\mathrm{m}^3/\mathrm{s}$ without wind stress and density gradients. The velocity is influenced by the water depth and bathymetric changes.

The cross-sections are both characterized by vertical uniform velocities, which decrease near the bottom up to zero due to the no-slip condition. Throughout the transect the velocities are positively signed, implying a downriver flow direction. The mean velocity increases with water depth, as expected due to equation (27). An exception is given at the western boundary of the estuarine mouth, where the velocity increases and becomes even greater than at the deepest transect position in the middle of the shipping channel.

The river changes its cross-section between the beginning of the eastern pier and the pier heads (compare with figure 12). This variation is asymmetric with respect to the shipping channel, leading to a higher increase of the cross-section area at the western side and afterwards greater decrease at the mouth of the river. Due to incompressibility of water a decreasing cross-section leads to an increasing flow velocity (jet effect):

$$v_1 \cdot A_1 = v_2 \cdot A_2 = const. \tag{37}$$

At the pier heads the decrease at the western side is greater than at the eastern side, leading to higher velocities. The jet effect is in addition responsible for the higher velocities in the transect at the middle of the river, due to its smaller cross-section area.

Vertical velocity profiles of the model for different river volume fluxes (solid lines) are compared with the analytical solutions of equation (27) (dashed lines) in figure 14 for the deepest transect points of the mouth of the river (left panel) and of the middle of the Warnow (right panel). Unlike the analytical solution, the velocity of the model results at the mouth are nearly uniform and increase near the ground, while the analytical solution grows logarithmically and becomes greatest at the surface. Similar results are obtained at the middle of the Warnow, with the difference that the velocity is even slightly decreasing near the surface.
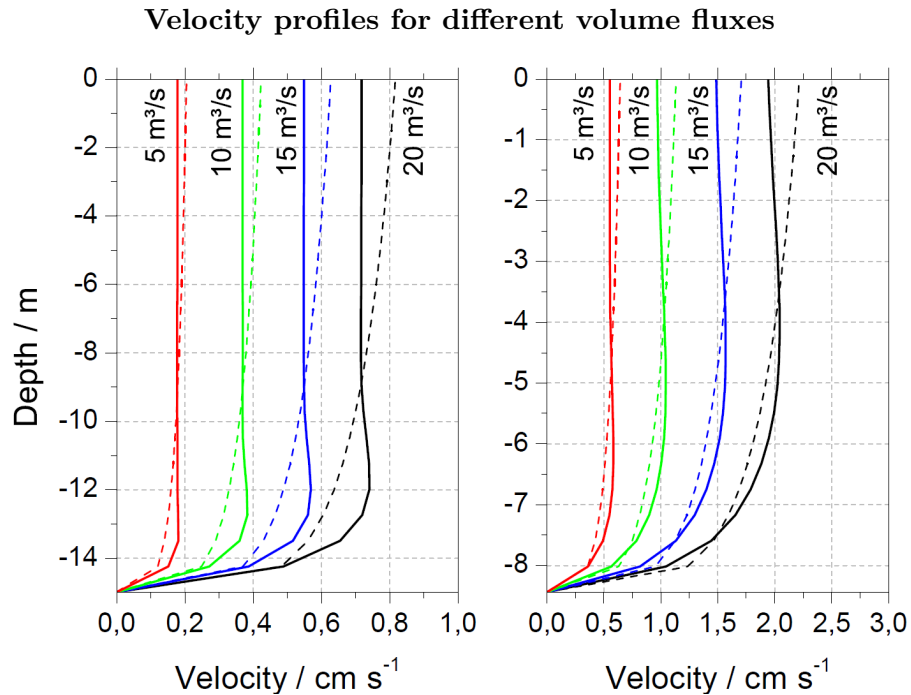
Velocity profiles for different volume fluxes

Figure 14: Vertical profiles of the velocity at the mouth (left panel) and in the middle of the river (right panel) for different river volume fluxes. The model results (solid lines) differ from the analytical solution (dashed lines) due to bathymetric changes.

For comparison vertical profiles in shallow areas are plotted in figure 15. The left panel belongs to a shallow position from the transect of the middle of the Warnow, while the right panel corresponds to the deepest position near the beginning of the river part. It can be seen, that the analytical solution fits the model results particularly at the beginning of the river while at a comparable water depth at the middle of the Warnow the behaviour resembles the profiles of figure 14.

This behaviour results from bathymetric changes along the river. While the cross-section area for the first 100 m is nearly constant, it changes its shape from then on continuously till the pier heads. These cross-sections can be subdivided into a lower part consisting of the shipping channel with a smaller cross-section area and an upper part enclosing the shallower areas with a higher cross-section area with respect to the channel. Whereas the shape and therefore the area of the channel is changing slowly, the upper cross-section area is steadily decreasing and increasing. This influences the velocity profile due to equation (37), which leads to the shown velocity profiles.
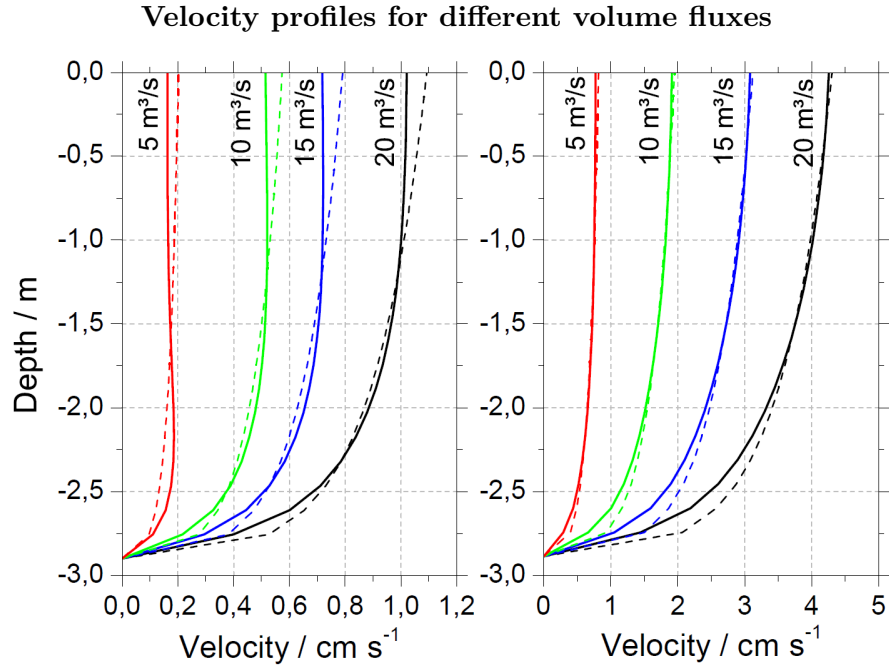
Velocity profiles for different volume fluxes

Figure 15: Vertical velocity profiles in the middle of the river (left panel) and at the origin (right panel) for different river volume fluxes. The model results (solid lines) fit with the analytical solution (dashed lines) at the origin in a better way, due to low bathymetric changes.

The deviance between numerical and analytical solutions becomes greater with higher velocities, as it can be seen in figure 14. Therefore the difference increases with higher river volume fluxes and with higher water depth (figure 16).

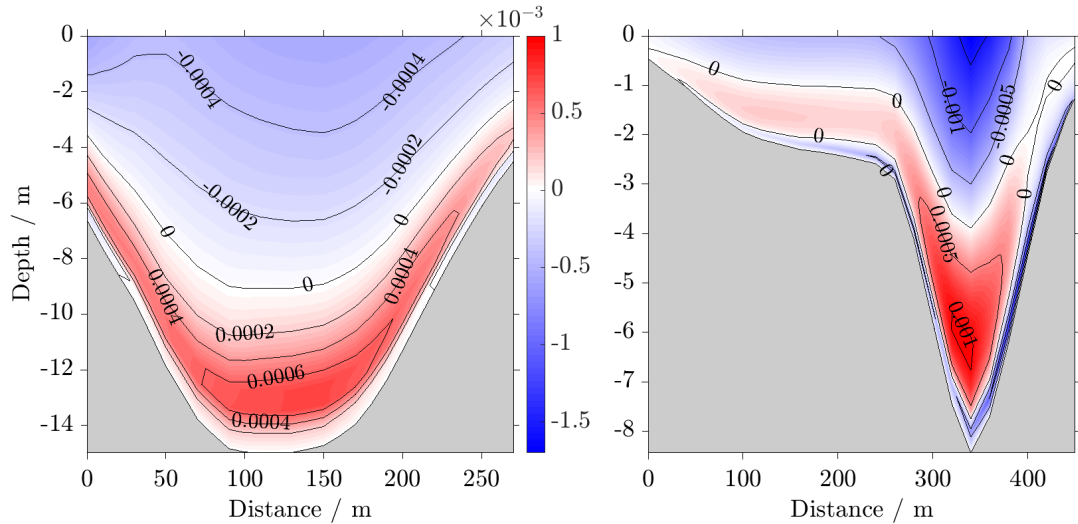**Absolute error between model results and analytical solution**

Figure 16: Difference between analytical solution and model results along the transect at the mouth (left) and in the middle of the river (right) for $Q = 10\,\mathrm{m^3/s}$. The divergence is greater where the water depth raises and the velocity becomes higher.

4.2   Wind induced velocities

The next test case considers pure wind straining without river inflow and density gradients. Wind induces momentum due to interaction with the water surface in the form of friction and atmospheric pressure. The resulting steady-state flow velocity profile under a northward wind field with $\tau = 0.20\,\mathrm{Pa}$ is shown in figure 17. Contrary to currents caused by river inflow, here additionally an upriver flow exists which is mainly located in the shipping channel. The wind drags water and causes a difference of the sea surface height which results in an opposite current due to the barotropic pressure gradient mentioned in equation (11). This is countered in the resulting residual flow as described in equation (28). The highest values of the velocity in the transect in the middle of the Warnow are higher than at the mouth which is caused by the smaller cross-section area and incompressibility of water as mentioned in section 4.1. The wind induced velocities are about two orders of magnitude higher than the velocities caused by pure river inflow, highlighting the role of wind straining in estuarine circulation. At the bottom the velocity becomes again zero due to the no-slip boundary condition.
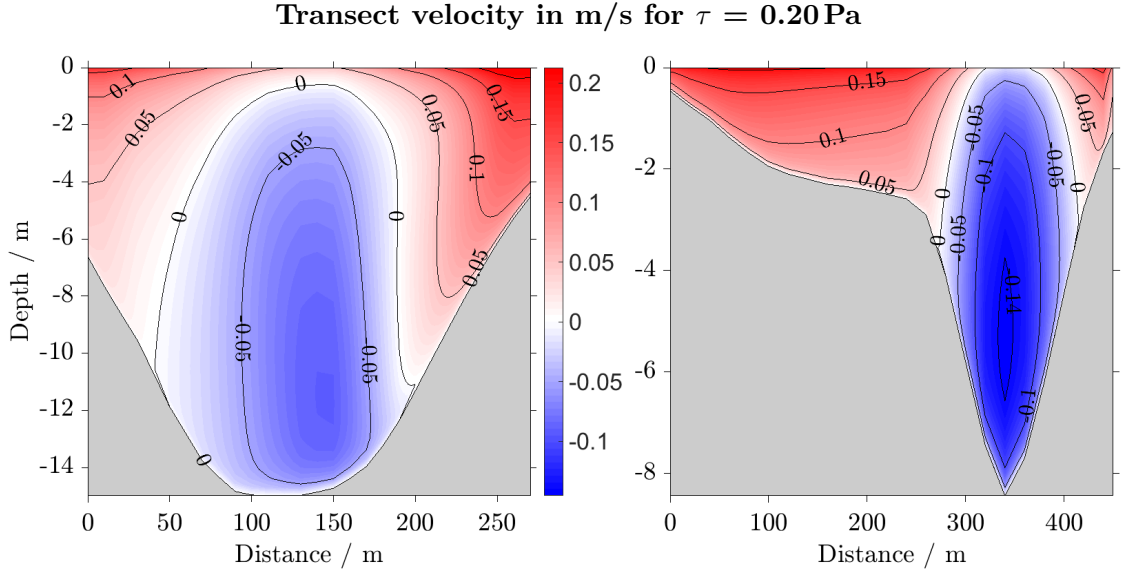
Transect velocity in m/s for $\tau = 0.20\,\mathrm{Pa}$

Figure 17: Velocity component perpendicular to the cross-section at the mouth of the river (left panel) and at the middle of the Warnow (right panel) for northward wind with $\tau = 0.20\,\mathrm{Pa}$. Additionally to the downriver component (red) an upriver current (blue) exists caused by the barotropic pressure gradient.

If the wind changes its direction, the water flow is influenced as well. The steady-state currents resulting from a southward wind field with $\tau = -0.20\,\mathrm{Pa}$ is shown in figure 18 for the mouth of the estuary in the left panel and for the middle of the Warnow in the right panel. As can be seen the velocity profile is now inverted with respect to the results of northward wind in figure 17. This matches with equation (27), where the wind stress τ behaves linearly in the wind straining term as well as in the residual flow u_r and therefore a changing sign of τ reverses the flow velocity.
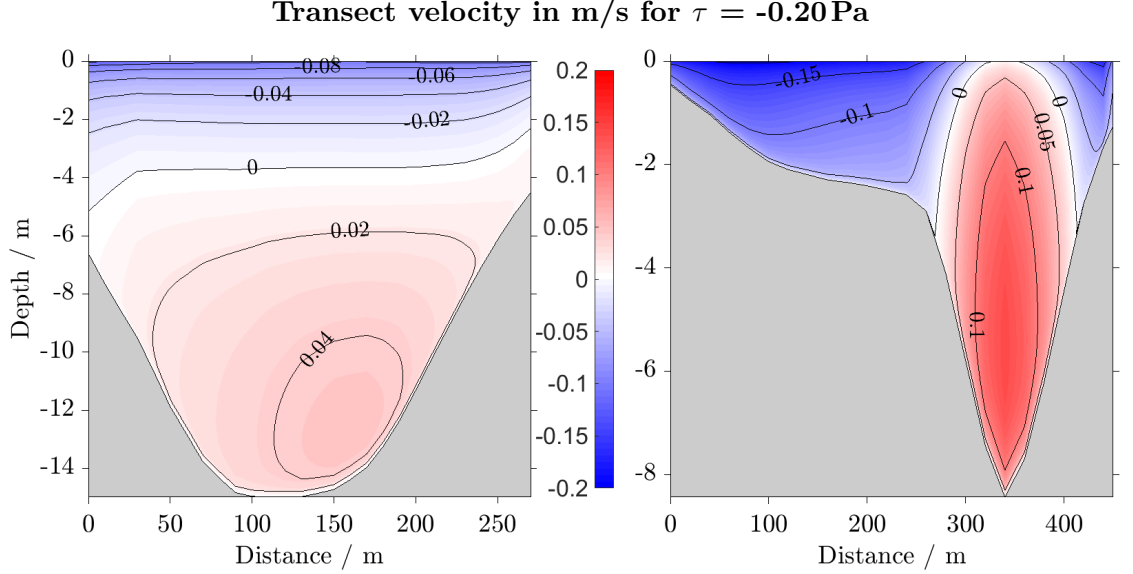
Figure 18: Velocity component perpendicular to the cross-section at the mouth of the river (left panel) and at the middle of the Warnow (right panel) for southward wind with τ = -0.20 Pa. The flow direction of the water is inverted with respect to northward wind fiels..

The shape of the solution is a superposition of the logarithmic wind straining component and the residual flow, governed by the sea surface slope and wind stress. The model results and analytical solutions with parabolic eddy viscosity are compared for weak and moderate northward wind velocities in figure 19. The bottom friction velocity u_*^b has been taken from model calculations and the residual flow u_r is calculated with equation (20). The basic behaviour of the analytical solution from equation (27) follows the numerical solution at the mouth of the river (left panel) and reproduces the right order of magnitude, but differs especially near the surface due to the singularity at $z = 0$. The situation is different with the transect at the middle of the Warnow (right panel). There the solutions assort well along the water column and only differ slightly in the surface and bottom layer. These distinctions can also be seen in figure 20, where the absolute error between the solution from equation (27) and the model result is shown for northward wind with τ = 0.20 Pa. The difference in the middle transect (right panel) is comparatively small with respect to that of the mouth of the river (left panel). Especially at the western boundary of the mouth transect the error becomes relatively high.

The quality in which the simplified analytical solution with parabolic eddy viscosity the model results reproduce depends on how good the profile assumed in equation (23) matches the viscosity calculated by the model. An overview about the viscosity obtained by the turbulent closure model and the absolute error with respect to equation (23) at the mouth of the river and at the middle of the Warnow is given in figure 21 and figure 22 respectively.

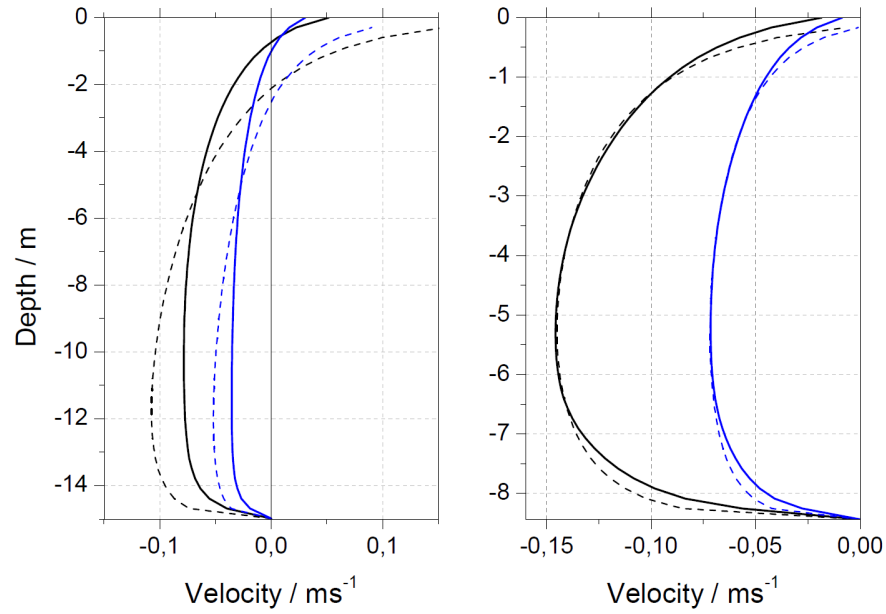**Velocity profiles in m/s for different wind stresses**

Figure 19: Vertical profiles of the flow velocity at the mouth (left panel) and in the middle of the river (right panel) for northwind wind with $\tau = 0.20\,\text{Pa}$ in black and $\tau = 0.05\,\text{Pa}$ in blue. The model results (solid lines) differ from the analytical solution (dashed lines) at the mouth due to distinctions of the eddy viscosity profiles.

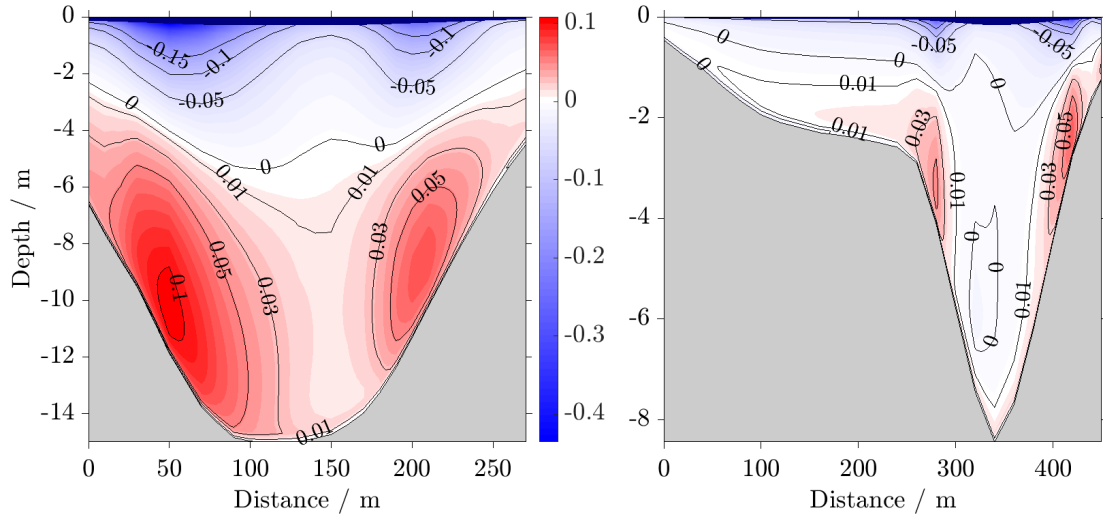**Absolute error between model results and analytical solution in m/s**

Figure 20: Difference between analytical solution and model results along the transect at the mouth (left) and in the middle of the river (right) for northward wind with $\tau = 0.20\,\text{Pa}$. The solutions match more accurately in the middle transect due to better conformance of numerical and analytical turbulent viscosities.

The maximal model eddy viscosity in figure 21 is shifted westward (left panel), while the maximum in the analytical solution (right panel) is located in the centre. Hence the distinction in figure 20 is greatest at the western side. Moreover the absolute values are lower in the analytical viscosity than in the model calculations, leading to the differences in the left panel of figure 19. The turbulent viscosity in the middle of the Warnow behaves
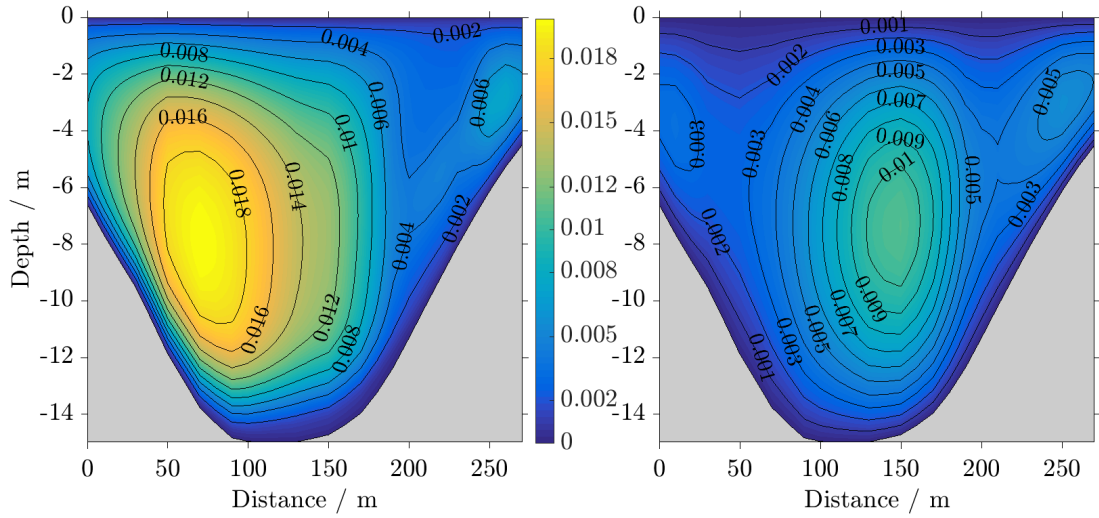
Numerical and analytical eddy viscosity in m^2/s

Figure 21: Turbulent viscosity ν_t calculated by the model (left panel) compared with the analytical solution of equation (23) at the mouth of the river for $\tau = 0.20$ Pa. The numerical results are shifted westwards and consist of higher values.

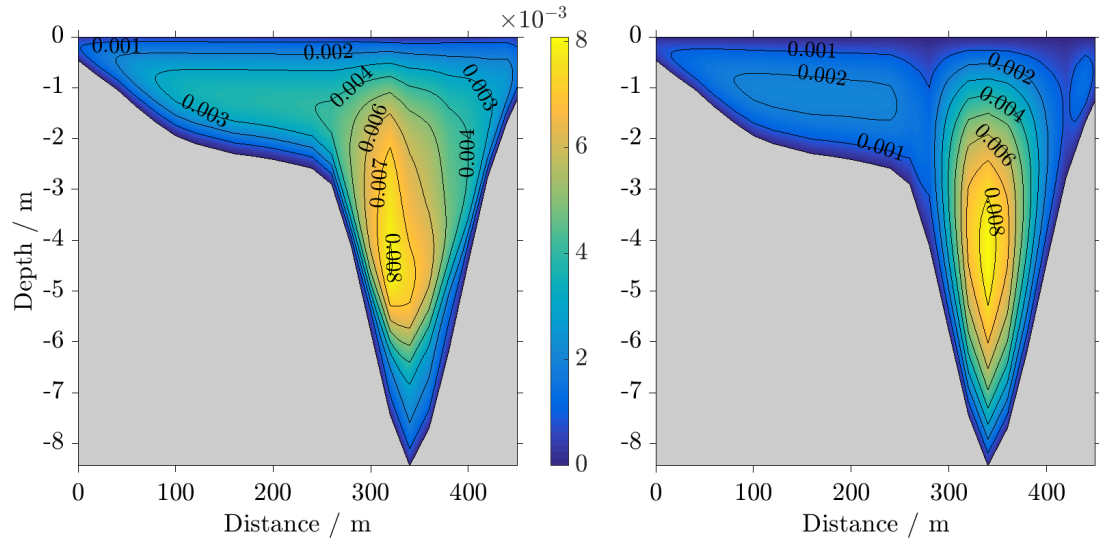## Numerical and analytical eddy viscosity in m^2/s

Figure 22: Eddy viscosity ν_t calculated by the model (left panel) compared with the analytical solution of equation (23) at the middle of the Warnow for $\tau = 0.20$ Pa. The solutions match more accurately than at the mouth of the river.

contrary to the mouth of the river. Here the analytical solution from equation (23) matches values calculated by the model more accurately in position as well as the range of values, leading to the close-fitting flow velocities in the right panel of figure 19.

4.3 Density driven flow

The last testcase considers density driven flows. Main contributer is the horizontal density gradient in equation (27). According to equation (12) a gradient of the buoyancy can be simply obtained due to differences in salinity. Therefore the salinity of the boundary was set to a constant value of 14 PSU, while the freshwater's salinity consists of 0.01 PSU. The river volume flux was set to $Q = 20\,\mathrm{m}^3/\mathrm{s}$. The experiments had shown that without additional forces only marginal horizontal gradients could be observed, because the river tended to flow over the layer of salty water without creating enough turbulent mixing. Therefore a southward wind with $\tau_w = -0.2\,\mathrm{Pa}$ was added in order to force vertical mixing. Here, too, the steady-state tended to reduce the gradients of salinity, therefore a snapshot in the adjustment time is presented in figure 23, for the mouth of the estuary on the left panel and for the transect in the middle of the Warnow on the right panel.
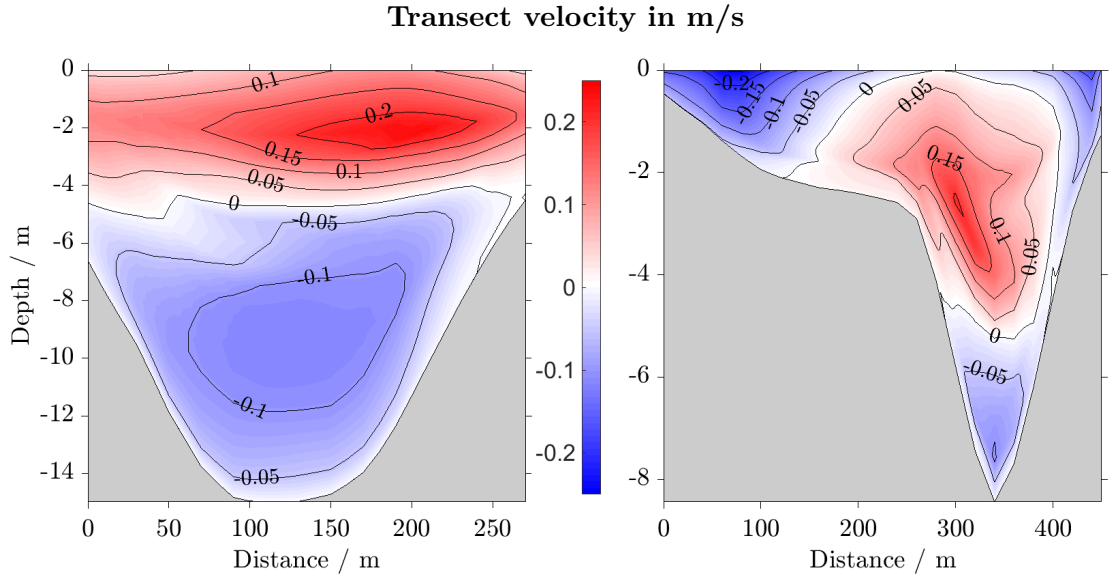
Transect velocity in m/s

Figure 23: Velocity component perpendicular to the cross-section at the mouth of the river (left panel) and at the middle of the Warnow (right panel) caused by density gradients between the river and the boundary. A southward wind with τ = -0.20 Pa was added to force vertical mixing. Additionally to the downriver component (red) an upriver current (blue) exists caused by the barotropic pressure gradient.

The influence of southward wind had been shown in figure 18 where an up-estuary wind field forces an upriver flow near the surface and a downriver current near the bottom. This effect can be slightly seen on the right panel where in shallower areas the water is transported up-estuary. Apart from this, the flow direction is opposite to the results of southward wind. At the surface less dense water flows to the ocean, while due to the bottom current salty water enters the river, as can be seen in figure 24. A down-estuary wind field would therefore amplify this estuarine circulation.
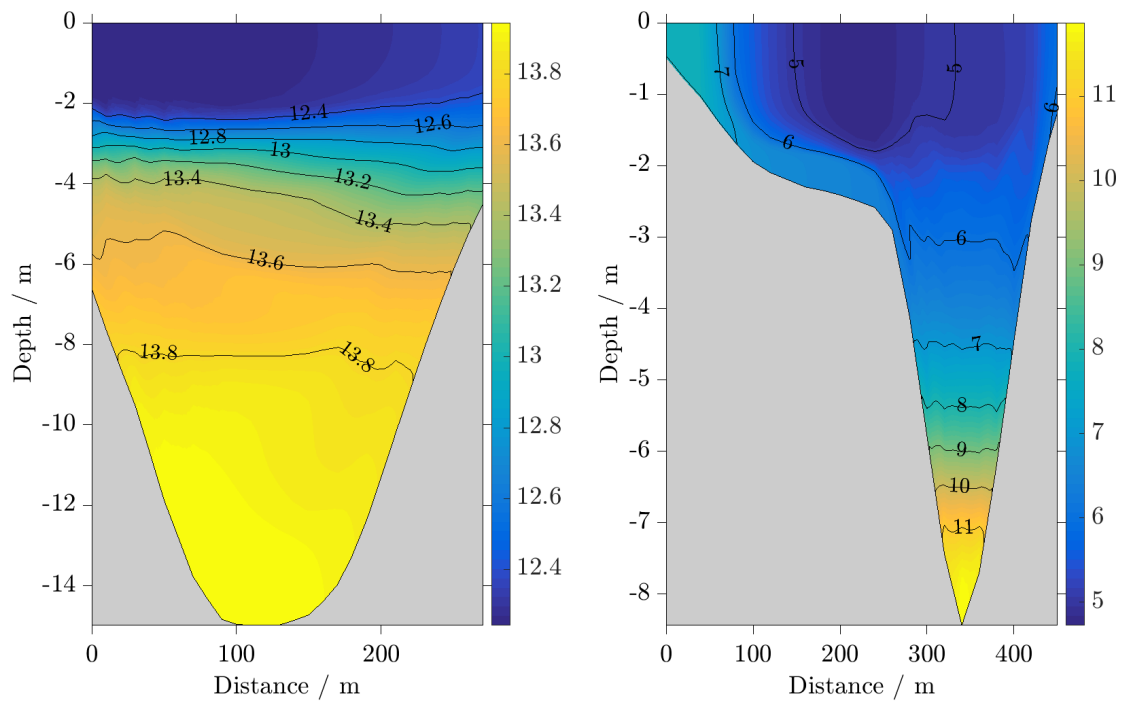
Figure 24: Transect salinity at the mouth of the river (left) and in the middle of the Warnow (right). The exchange flow transports salinity from the ocean into the river.

5 Results of realistic simulations

In the following the results of realistic simulations of the year 2014 are presented. The simulation starts in the second half of the year 2013 to provide an adjustment time for the essentially run. The results will be discussed, mainly using the example of March.

Figure 25(a) shows the wind data of March 2014, from Germany's National Meteorological Service, the Deutscher Wetterdienst (DWD), in the area of the mouth of the river. The absolute wind velocity in a height of $10\,\mathrm{m}$ is plotted as a straight line and the corresponding wind directions are shown as circles. Special events in this month are the storm front EV on 14 / 15 March and the deep depression FELIZ on 16 / 17 March.

Due to the north-south orientation of the Warnow, wind velocities aligned in this direction become special drivers of estuarine circulation. A phase with relatively constantly northward blowing wind is given from 6 - 10 March. Southward wind can be found on the 11th and from 24 - 25 March respectively, with a mean velocity of $4\,\mathrm{m/s}$. Because wind drags water when it blows over the sea surface, this changes the elevation of the water level. As it can be seen in figure 25(b) in red, in times of northward wind fields the sea surface height (SSH) is lower than the annual average, while southward wind bottles water up in the estuary, which can be seen especially on 26 March. For comparison the changes of salinity $s' = s - <s>_t$ are shown, each averaged over the area of the transect in the middle of the Warnow. It can be seen, that an increasing surface elevation forces an increase of salinity and a decreasing sea surface height decreases the salinity and therefore the density. The temporal progress of the spatially averaged potential densities at different positions are compared in figure 25(c).
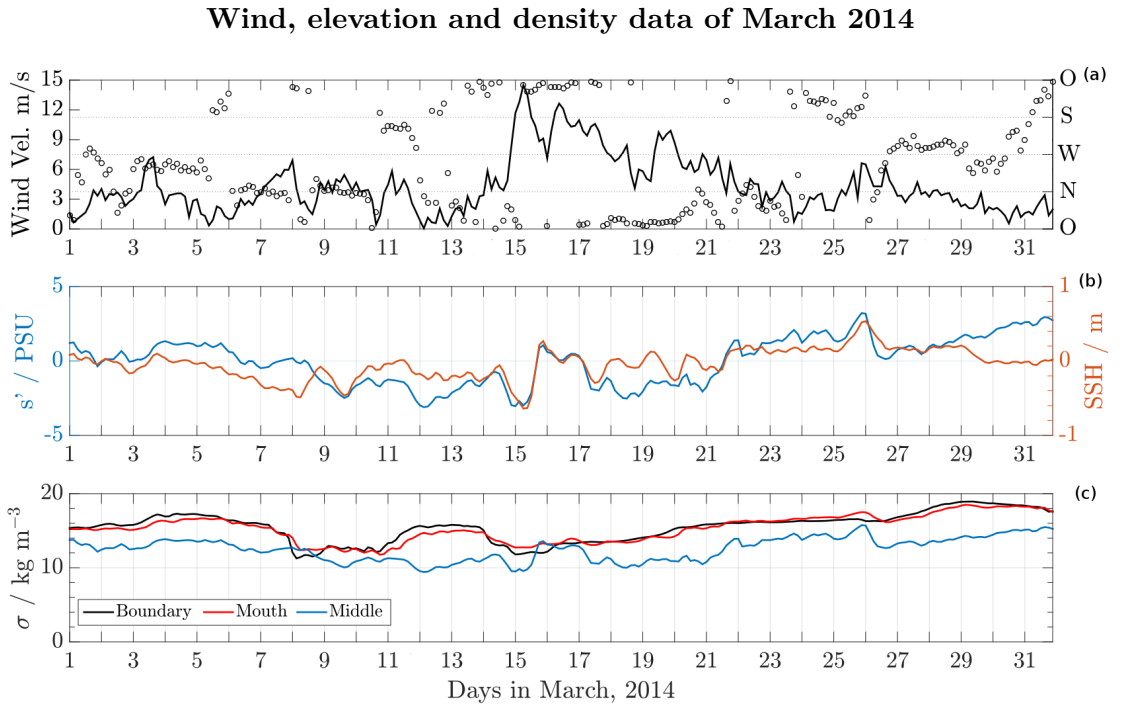
Wind, elevation and density data of March 2014

Figure 25: Upper panel: Black line showing absolute wind velocity in m/s with the corresponding wind direction in circles. Middle panel: Sea surface height (SSH) in m compared with the changes of salinity in the middle transect. A raise in sea level correlates with an increase of salinity. Lower panel: Spatial averaged potential density σ in kg/m^3 at the boundary (black), at the mouth of the river (red) and in the middle of the Warnow (blue).

The black line corresponds to the boundary of the model, while the red and blue one belongs to the mouth of the river and the middle of the Warnow, respectively. In general the density is lower in the Warnow than at the boundary due to freshwater inflow of the river, but there are cases, where at the mouth and even in the middle of the Warnow higher densities can be found (e.g. on the 8th of March), which influences the strength and direction of the density driven estuarine circulation.
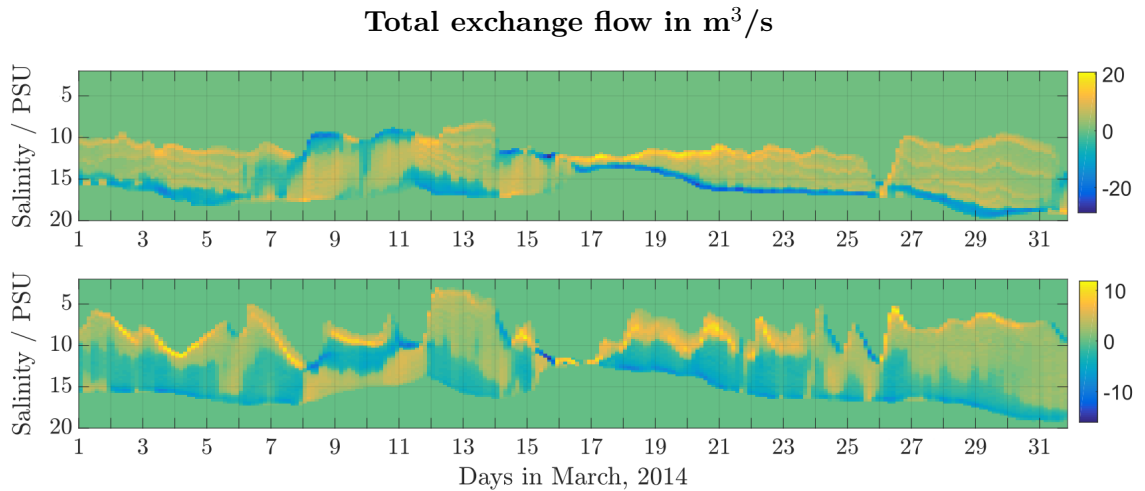
Total exchange flow in m^3/s

Figure 26: Total exchange flow in March 2014 at the mouth of the river (upper panel) and in the middle of the Warnow (lower panel). In general, outward streaming water (yellow) consists of lower salinity, while upriver currents (blue) transport higher salinity into the estuary. The estuarine circulation is inverted in times where the vertically averaged density of the water in the river is higher than at the boundary.

The transport of salinity in and out of the transect can be characterized by the concept of total exchange flow as explained in chapter 2.3. In figure 26 the TEF is shown at the mouth of the river (top) and in the middle of the Warnow (down). For this purpose the water of the transect is divided into salinity classes (y-axis). The resulting volume flux of water in a specific salinity class is shown in yellow for downriver and in blue for upriver transports. In general salty water flows upriver, while less dense water streams downriver due to density gradients as expected from experiments in chapter 4.3. This behaviour is reversed in special situations when the density at the mouth becomes higher than at the boundary where the interaction is mainly given through the shipping channel. This occurs on 8 - 11, 14 - 16 and 26 March, as can be seen in figure 25(c). On the 8th this is even the case although the wind is blowing northward and therefore increasing estuarine circulation. The density gradients are strong enough to invert the flow directions as shown in figure 27 for the mouth of the river (left) and in the middle of the Warnow (right). On 10 March an inflow exists in all salinity classes, meaning an upriver current affecting the whole water column, as a result of changes in the sea surface height of about 0.5 m in a half day. After that the density at the mouth is comparable to that of the boundary, which decreases the influence of the density gradient term in equation (24). Therefore the beginning southward wind on 11 March can in turn inverse the estuarine circulation.

The TEF looks slightly different at the middle of the Warnow (figure 26(b)). The range of the salinity classes is higher than at the mouth due to freshwater inflow and mixing with salty water from the bottom. Therefore the upriver current is not limited to high salinities as it can be seen for the mouth of the river from 17 to 26 March in figure 26(a). In general the density of the water in the middle transect is lower than at the boundary with exception of day 8 and 15 / 16 as can be seen in figure 25(c). Coincident with the mouth of the river the estuarine flow is inverted on these days. Surprisingly sensitively

reacts the flow under changes of the wind direction due to the small water depth in the middle of the Warnow. Here the estuarine circulation is inverted due to southward wind fields for example on day 6, 11 and 24 - 26.
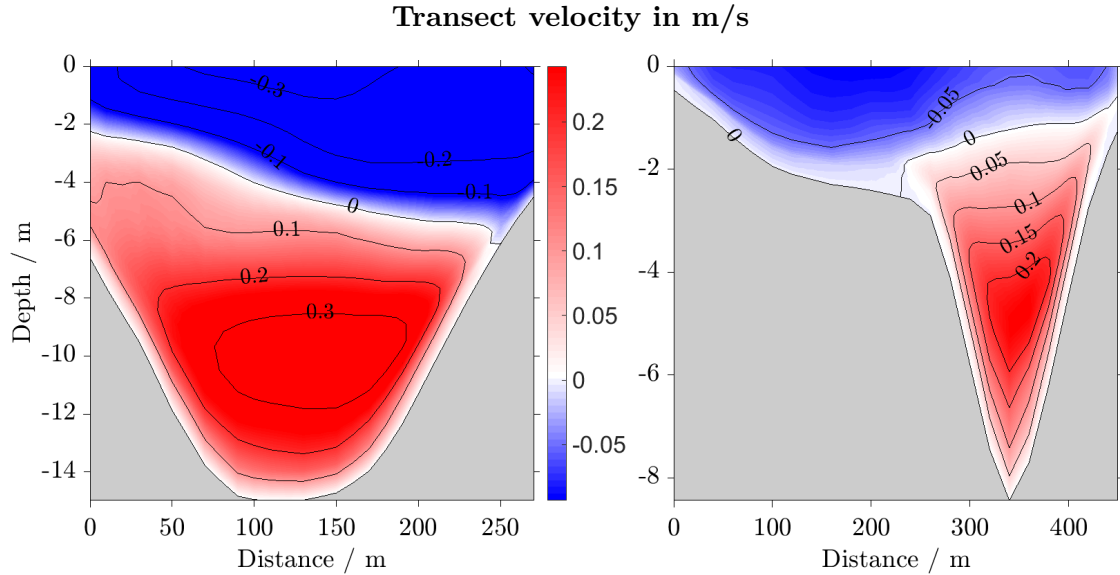

Figure 27: Transect velocity at the mouth of the river (left panel) and at the middle of the Warnow (right panel) on 8 March in m/s. Different from the results in chapter 4.3, the upriver flow is located at the surface, while the downriver current is near the bottom. This inversion is caused by a negative density gradient with respect to the boundary.

The northward velocity component of the water current along the transect is shown in figure 28 for a time series from 7 to 12 March. Negative values in blue belong to an upriver flow direction, while the positive currents in red correspond to downriver flows. On day 7 a common estuarine flow situation is shown. A downriver current is located at the surface, while an upriver flow at the bottom is driven by density gradients. In the intermediate layer, where the velocity changes its direction, the water currents produce shear stress due to vertical gradients of the velocity, which drives turbulent mixing and therefore a vertical transport of salinity. As can be seen in figure 25(c), the estuarine circulation is inverted on 8 March due to the higher density in the estuary and lower density outside, leading to a negative density gradient. Due to inversion of the velocity direction, surface water with lower salinity is flowing into the estuary, while salty water near the bottom is pushed outward. The incoming water mixes with the freshwater inflow of the river and reduces the salinity in the Warnow, leading to the salinity profiles for day 7 to 11 in figure 29. On 9 and 10 March an additional downriver flow occurs at the surface as a result of the low density freshwater inflow, leading to a tripartite vertical velocity profile. The decreasing salinity in the estuary reduces the density and therefore extenuates the compensation current, until the densities inside and outside the estuary are comparable (figure 25(c)). The normalization process is interrupted by the appearing southward wind field on day 11, on its part increasing the inverted estuarine circulation again. On 12 March the density in the river becomes lower than at the boundary (figure 25(c)) and the wind changes direction, leading to the currents in figure 28, which describes the normal estuarine circulation analog to day 7. Therefore a dense bottom current enters the estuary in the shape of a salt water plume, as shown on day 12 in figure 29, concerting with the TEF behaviour in figure 26.
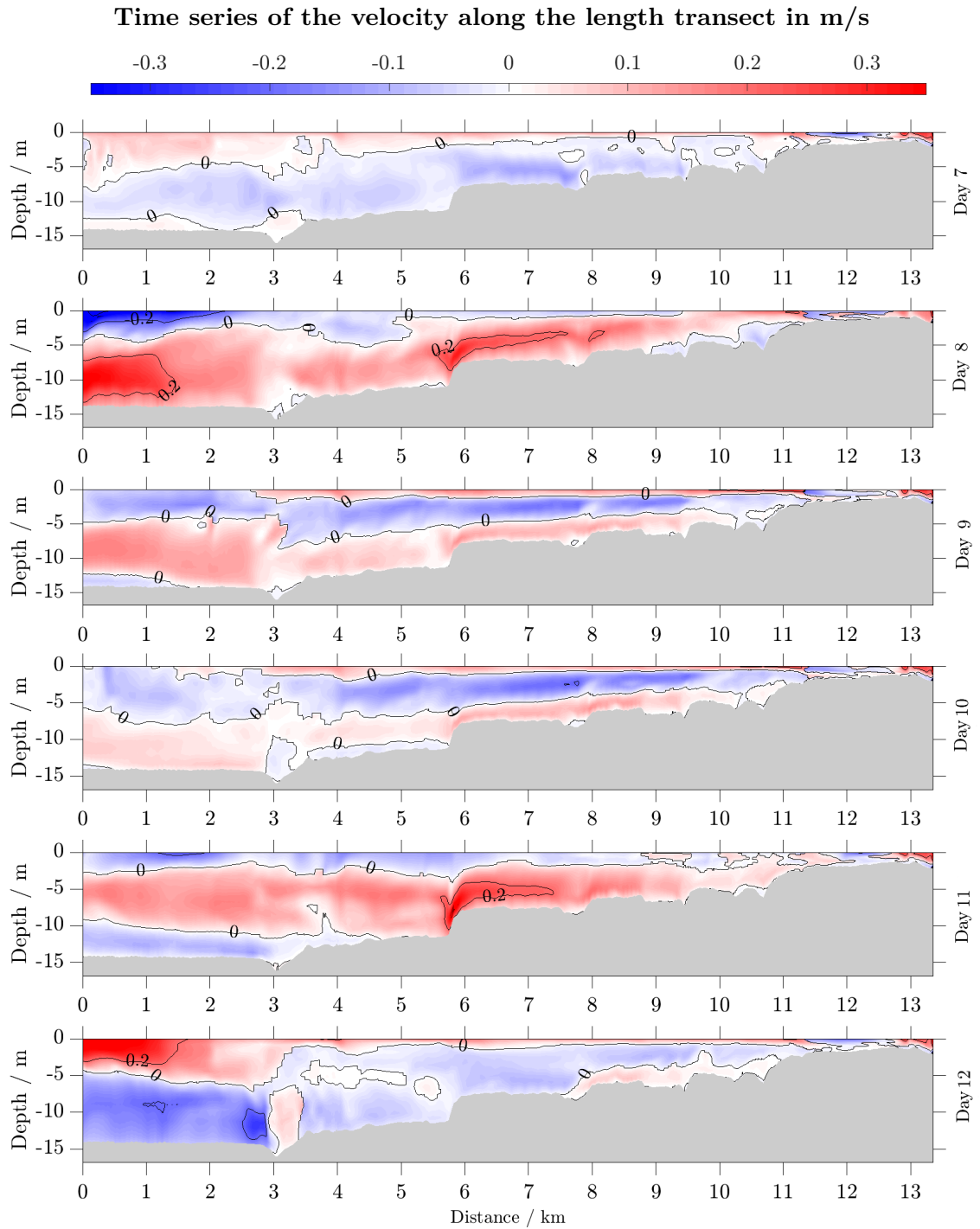
Figure 28: Northward velocity component in m/s along the transect on 7 - 12 March. The mouth of the river is located on the left side and the origin on the right side. The estuarine circulation is inverted on the 8th day due to negative density gradients between the river and the ocean. Therefore water flows at the surface in upriver direction (blue) and near the bottom in downriver direction. On day 11 southward wind fields amplify this effect. This process is stopped due to inversion of the density gradient.
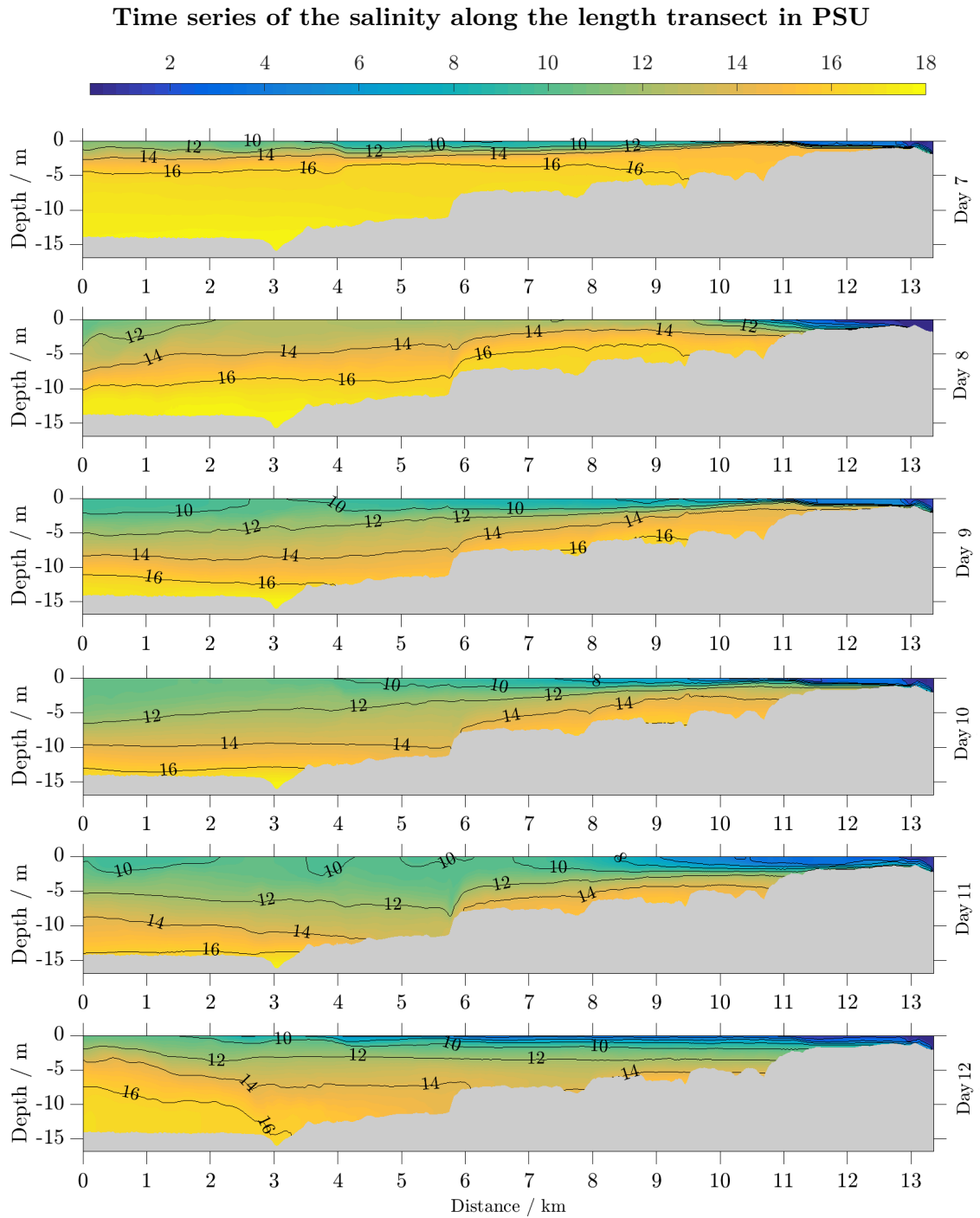
Figure 29: Salinity profile in PSU along the transect on 7 - 12 March. Due to inversion of the estuarine circulation less dense surface water is transported into the river, while the downriver near bottom currents move salty water outward. Therefore the salinity in the Warnow is reduced, which inverts the density gradient just as the velocity direction, leading to the salt water plume at the bottom on day 12.

6 Validation

In the following the model results are compared with measurements executed throughout the year 2014. Available validation data are namely the water level in Warnemünde and a time series of vertical salinity and temperature profiles near the mouth of the river. Temperature and surface elevation profiles could be well reproduced, in salinity some divergences appear.

6.1 Surface elevation

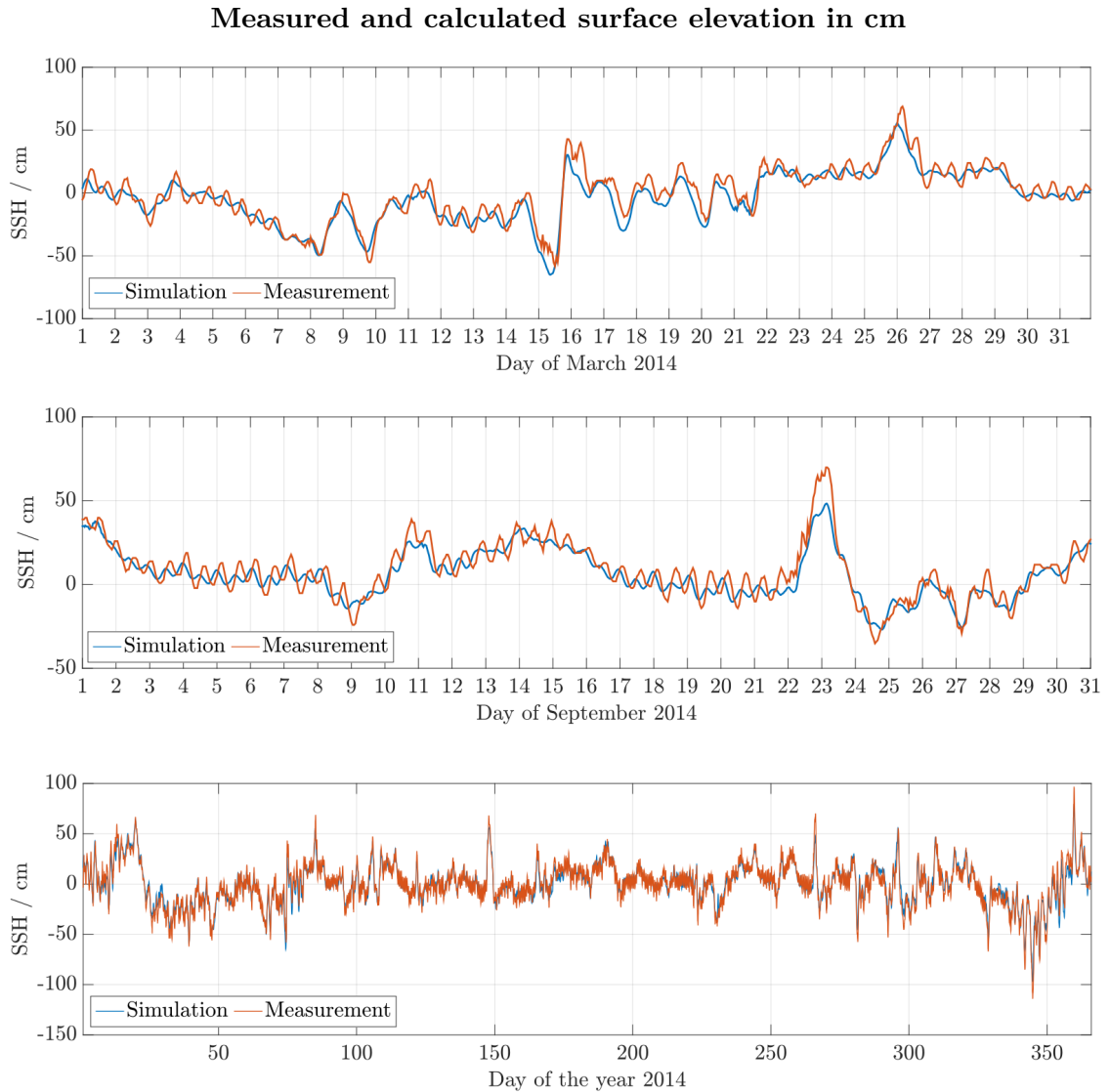**Measured and calculated surface elevation in cm**

Figure 30: Measured sea surface height in red and model results in blue are compared by way of example for March and September in the upper panels and for the complete year 2014 in the lower panel. The general behaviour could be reproduced, but the model results show a smoothed shape with respect to the measurements.

The surface elevation of the model results and the measured data provided by the German Federal Maritime and Hydrographic Agency are compared in figure 30 for the month March and September just as for the whole year 2014 in hourly resolution. For that the means of the data sets were calculated and subsequently subtracted from them. It can be seen that the general behaviour of the water level could be reproduced in the model, mainly by the good elevation data at the boundary provided by the used Baltic Sea model. The tidal amplitude as well as some peak values could not be resolved, leading to a smoothed curve with an acceptable root-mean-square error of 7.18 cm in March, 8.07 cm in September and 7.99 cm in the year 2014.

6.2   CTD - Measurements

Data sets of vertical salinity and temperature profiles near the mouth of the river are provided by the Leibniz Institute for Baltic Sea Research (Warnemünde), recorded with a manual CTD-instrument (Conductivity, Temperature, Depth). The measured salinity profiles are compared with the model results in figure 31. Times without measured data are left blank. The temporal and vertical progress of the model salinity coincides well with the measured data at several times. On the one hand even singularities such as on day 90 and day 150 could be reproduced, but on the other hand the absolute values of salinity differ between numerical solution and the recorded profiles. The model results tend to be higher than the validation data as it can be seen around day 25 and day 200. The RMSE of measurements and simulations (vertically averaged) in March is 1.6 PSU and amounts to 3.7 PSU in the year 2014.
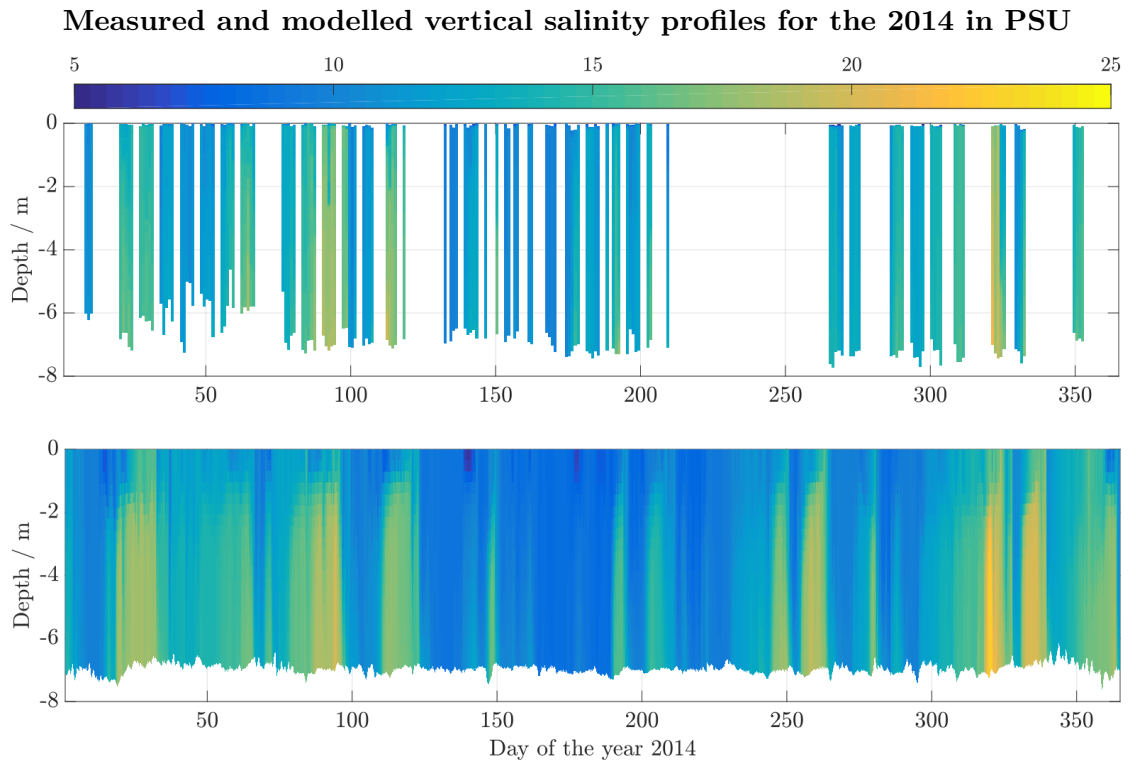

Figure 31: Measured vertical salinity profiles from data sets of a CTD (upper panel) compared with the model results (lower panel) for the year 2014 in PSU. The temporal behaviour could be reproduced by the model. The vertical values of the model tend to be higher than the measurements.

The measured temperature profiles in figure 32 show a seasonal variability along the year and vary only slightly throughout the water column. The highest temperatures can be observed in the middle of the year, while the lowest appear in January and February. The model results (lower panel) mirror the temporal behaviour of the measurements at the right times just as the absolute values, whereby the RMSE of measurements and simulations (vertically averaged) in March is $0.88\,°C$ and amounts to $0.67\,°C$ in the year 2014. This can be seen as well in figure 33. Here the temporal variability of salinity (upper panel) and temperature (lower panel) are shown for a water depth of $3\,m$. The numerical temperature of the model in blue corresponds well with measurements in red and differ only marginally with a RMSE of $0.8\,°C$. The salinities match during the months of March to April and from end of October to December. Over the first half of the year the salinity in the model tends to be higher than the measurements, while during the second one the numerical solutions are too low. Rising and falling behaviour could be reproduced. The RMSE for the salinity of 2014 is $1.7\,°C$ and therefor acceptable.

Measured and modelled vertical temperature profiles for 2014 in °C
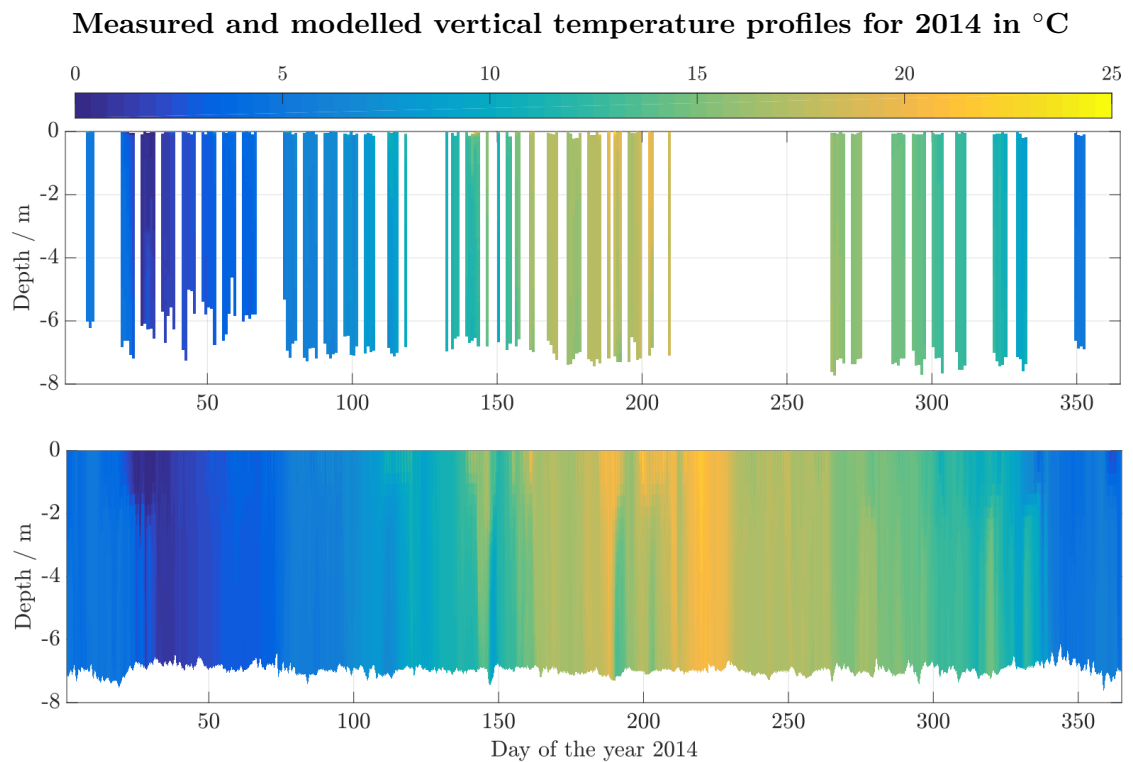

Figure 32: Measured vertical temperature profiles from data sets of a CTD (upper panel) compared with the model results (lower panel) for the year 2014 in °C.
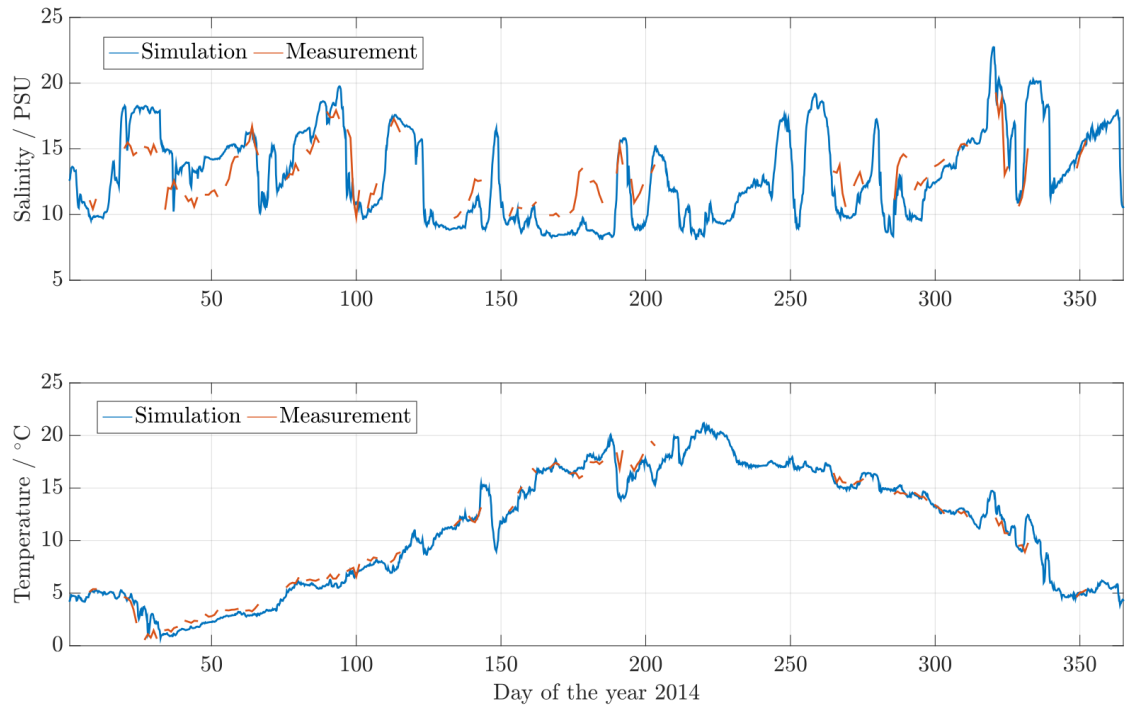
Figure 33: Upper panel: Measured salinity in red compared with model results in blue for a water depth of 3m. The salinities match during the months of March to April and from end of October to December. Lower panel: Measured salinity in red compared with model results in blue for a water depth of 3m. The data match well both in behaviour and absolute values.

7   Conclusion and outlook

An analytical solution for wind driven estuarine circulation with parabolic turbulent viscosity could be derived under the assumption of a zero surface roughness length. The equation has a logarithmic character which was verified with different idealised test-cases with the bathymetry of the Warnow. Although simplified assumptions were used, this solution reproduced the numerical results satisfiable if their respective viscosity profiles matched.

The proceedings in the river Unterwarnow could be successfully simulated and validated for the year 2014 by the use of the coastal ocean model GETM. Due to the negligible tidal influences this estuary is governed mainly by the density gradients between the river and the ocean just as by wind straining effects. It could be shown, that the estuarine circulation can be inverted if the density in the river is higher than in front of the mouth of the river and during times of up-estuary blowing wind fields if the density gradient is weak. This is mainly researched on the basis of a validated month by evaluation of the velocity and salinity profiles during a cycle of inversion and normalization of the flow direction. The time series of measured temperature and elevation data could be well reproduced by the model, while the salinity differs at some times.

In following studies the created model of the Warnow will be used for several particle tracking experiments. These will be executed for instance with microplastics particles to research if hot spots of accumulations can be found in the coastal area of Rostock and if observed discoveries can be retraced to supposed sources like the defecator of Rostock. Similar experiments will be done with *Escherichia coli* bacteria.

Therefore, in a first step the coastal line in the model will be extended to a total amount of about 20 km. For that reason the used bathymetry will be modified in a second step by the use of a curvilinear coordinate system, so that nearby coastal areas can still be highly resoluted with a grid spacing of 20 m and further afar areas are resolved with a rougher spatial resolution in order to limit the number of grid points to a reasonable level. Then perhaps an adjustment test should be done to find the optimal number of subdomains with the lowest total wall-clock time, because an increasing number of subdomains leads at some point to an overproportional growing of communication time between the tasks. The number of vertical layers should only be increased if the opportunity exists to run the model at a major computer cluster. The use of vertical adaptive coordinates instead of vertical sigma coordinates could be trialed for comparison. Moreover, the missing yacht harbour in Hohe Düne has to be added to the bathymetry and the heights of the islands of Pagenwerder have to be adjusted to enable possible flooding of these areas.

It is worth considering to start the simulations at the end of 2012, with the result that the influence of the european windstorm Xaver in December 2013 can be studied in the Warnow estuary which had been subjected to sea level differences of about 2m in one day at this event.

Appendix

Derivation of an analytical expression for wind driven estuarine circulation with a parabolic eddy viscosity

Inserting the parabolic viscosity profile

$$\nu_t = \kappa |u_*^b|(z + z_0^b + H)\left(-\frac{z}{H}\right),$$ (38)

into the differential equation for the depth dependent velocity

$$\partial_z u = \frac{g\partial_x \eta}{\nu_t}z + \frac{\partial_x b}{2\nu_t}z^2 + \frac{\tau_w}{\nu_t \rho_0},$$ (39)

leads to

$$\partial_z u = -\frac{g\partial_x \eta H}{\kappa|u_*^b|}\frac{1}{z + z_0^b + H} - \frac{\partial_x b H}{2\kappa|u_*^b|}\frac{z}{z + z_0^b + H} - \frac{\tau_w H}{\rho_0 \kappa |u_*^b|}\frac{1}{z^2 + z(z_0^b + H)}$$ (40)

The vertical integral from the bottom $-H$ to an arbitary position z in the water column reads with the integrals

$$\int_{-H}^{z'} \frac{1}{z + z_0^b + H}\mathrm{d}z = \ln\left(\frac{z + z_0^b + H}{z_0^b}\right) = \ln(D),$$ (41)

$$\int_{-H}^{z'} \frac{z}{z + z_0^b + H}\mathrm{d}z = (z + H) - (z_0 + H)\ln(D),$$ (42)

$$\int_{-H}^{z'} \frac{1}{z^2 + z(z_0^b + H)}\mathrm{d}z = \frac{1}{z_0 + H}\left(\ln\left(\frac{z}{-H}\right) - \ln(D)\right)$$ (43)

as:

$$u(z) = -\frac{g\partial_x \eta H}{\kappa|u_*^b|}\ln(D) - \frac{\partial_x b H}{2\kappa|u_*^b|}\left((z + H) - (z_0 + H)\ln(D)\right) - \frac{\tau_w H}{\rho_0 \kappa|u_*^b|}\frac{1}{z_0 + H}\left(\ln\left(\frac{z}{-H}\right) - \ln(D)\right),$$ (44)

where the no-slip condition $u(-H) = 0$ is used. Calculation of the residual flow

$$u_r = \frac{1}{H}\int_{-H}^{0} u\mathrm{d}z,$$ (45)

with the integrals

$$\frac{1}{H}\int_{-H}^{0}\ln(D)\mathrm{d}z = \frac{z_0^b + H}{H}\ln\left(\frac{z_0^b + H}{z_0^b}\right) - 1 = C$$ (46)

$$\frac{1}{H}\int_{-H}^{0}(z + H)\mathrm{d}z = H/2$$ (47)

$$\frac{1}{H}\int_{-H}^{0}\ln\left(\frac{z}{-H}\right)\mathrm{d}z = -1$$ (48)

leads to:

$$u_r = -\frac{gH\partial_x \eta}{\kappa|u_*^b|}C + \frac{\partial_x b H^2}{2\kappa|u_*^b|}\left(\frac{z_0 + H}{H}C - \frac{1}{2}\right) + \frac{\tau_w}{\rho_0 \kappa|u_*^b|}\frac{H}{H + z_0}(1 + C).$$ (49)

This resolved for the sea surface slope $-g\partial_x \eta$ and subsequently inserted into equation (44), which leads to the final solution

$$u(z) = \frac{\partial_x b H^2}{2\kappa|u_*^b|}\left[\frac{1}{2C}\ln\left(\frac{z + H + z_0^b}{z_0^b}\right) - \left(\frac{z}{H} + 1\right)\right] + \frac{1}{C}\ln\left(\frac{z + H + z_0^b}{z_0^b}\right)u_r$$ (50)

$$- \frac{\tau_w}{\rho_0 \kappa|u_*^b|}\frac{H}{H + z_0^b}\left(\ln\left(\frac{z}{-H}\right) + \frac{1}{C}\ln\left(\frac{z + H + z_0^b}{z_0^b}\right)\right) \quad .$$

References

Arakawa, A., and V. R. Lamb, 1977:*Computational design of the basic dynamical processes of the UCLA General Circulation Model*, Meth. Comput. Phys., pp. 173–263.

Beckers, J.-M., and E. Deleersnijder, 1993: *Stability of a FBTCS scheme applied to the propagation of shallow-water inertia-gravity waves on various space grids*, J.Comp.Phys.,108, 95–104.

Burchard, H., Bolding, K., 2002: *GETM - a general estuarine transport model.* Scientific documentation. Technical Report EUR 20253 EN. Tech. rep., European Commission., Ispra, Italy.

Burchard, H., Bolding, K., Villarreal, M. R., May 2004: *Three-dimensional modelling of estuarine turbidity maxima in a tidal estuary.*, Ocean Dynamics 54 (2), 250–265.

Burchard, H. and R. D. Hetland, 2010:*Quantifying the contributions of tidal straining and gravitational circulation to residual circulation in periodically stratified tidal estuaries.* J. Phys. Oceanogr., 40, 1243–1262.

Burchard, H., R. D. Hetland, E. Schulz, and H. M. Schuttelaars, 2011: *Drivers of residual circulation in tidally energetic estuaries: Straight and irrotational estuaries with parabolic cross-section.* J. Phys.Oceanogr., 41, 548–570.

Hansen, D. V. and M. Rattray, 1965: *Gravitational circulation in straits and estuaries.* J. Mar. Res., 23, 104–122.

Knudsen, M., 1900: *Ein hydrographischer Lehrsatz.* Ann. Hydrogr. Mar. Meterol., 28, 316–320.

MacCready, P., 2011:*Calculating Estuarine Exchange Flow Using Isohaline Coordinates.* Journal of Physical Oceanography 41 (6),1116–1124.

Danksagung

Mein Dank gilt meinem Betreuer Prof. Hans Burchard sowie der ganzen Arbeitsgruppe, die ihre Zeit und ihr Wissen gerne mit mir teilten und mir die Möglichkeit gaben viel interessantes über meine Masterarbeit hinaus zu lernen und ausprobieren zu dürfen. Ich danke von Herzen meiner geduldigen Frau und meiner Familie, die mich im Studium in jeder Art und Weise unterstützte.

Selbstständigkeitserklärung

Ich versichere hiermit an Eides statt, dass ich die vorliegende Arbeit selbstständig angefertigt und ohne fremde Hilfe verfasst habe, keine außer den von mir angegebenen Hilfsmitteln und Quellen dazu verwendet habe und die den benutzten Werken inhaltlich und wörtlich entnommenen Stellen als solche kenntlich gemacht habe.

Rostock, 08. Oktober 2015